Diplomarbeit

Intraband Spectroscopy of Semiconductor Quantum Dots

Alexander Weber

Physikalisches Institut der
Julius-Maximilians-Universität
Würzburg

Institut d'Électronique Fondamentale,
Orsay

August 1998

Contents

1 Introduction **1**

2 Theory **4**

2.1 Wavefunction in quantum structures 4

2.1.1 3D bulk material 4

2.1.2 2D quantum well 5

2.1.3 1D quantum wire 10

2.1.4 0D quantum dot 10

2.2 Density of states 14

2.3 Optical transitions 15

2.3.1 Dipole moment and selection rules 18

2.3.2 Oscillator strength 21

2.3.3 Intraband absorption 21

2.3.4 Temperature dependance 22

3 Sample growth and AFM characterization **25**

3.1 Stranski Krastanov growth 25

3.2 Sample description 26

3.3 AFM characterization 27

4 Experimental setup **30**

4.1 Photoluminescence 30
4.2 Photoluminescence excitation 32
4.3 Intraband absorption 32
4.3.1 FTIR spectrometer 32
4.3.2 Photo-induced experiments 34
4.3.3 Background spectra 35

5 Photoluminescence results 37
5.1 Photoluminescence 37
5.1.1 Uniformity of the sample 39
5.1.2 Influence of excitation power 39
5.2 Photoluminescence excitation 42
5.3 Conclusion 43

6 Intraband spectroscopy 44
6.1 Photo-induced intraband absorption of the n.i.d. sample 44
6.1.1 Zigzag configuration 44
6.1.2 Background 46
6.1.3 Confirmation of the absorption in different configurations 47
6.1.4 Normal incidence 48
6.1.5 Conclusion 49
6.2 Intraband absorption of the doped samples 51
6.2.1 Influence of temperature 53
6.2.2 Polarization-angle dependence 53
6.2.3 Influence of doping density 54
6.2.4 Conclusion 55
6.3 Spontaneous emission 56
6.4 Conclusion 58

7 Conclusion **59**

A Material parameters **61**

References **63**

List of Figures

2.1 Scheme of the band structure of InAs / $In_{0.52}Al_{0.48}As$. 5

2.2 Effects of biaxial strain: decrease of the degeneracy of the valence band and change of the effective masses. 9

2.3 Strain distribution in an InAs quantum dot 12

2.4 The electronic structure of a strained InAs pyramidal quantum dot embedded within GaAs. 13

2.5 Schematic representation of the energy dependence of the density of states for 3D, 2D, 1D and 0D systems. 15

2.6 Interband and intraband transitions for quantum wells, quantum wires and quantum dots. 16

3.1 Sample layer schemes. 28

3.2 AFM image of an uncapped InAs / $In_{0.52}Al_{0.48}As$ sample. 29

4.1 Scheme of the PL experiment setup. 31

4.2 Sample in a 45 ° waveguide configuration. 35

4.3 Experimental setup for infrared experiments. 36

5.1 PL of the n.i.d. sample M400 at $T = 4.2$ K. 38

5.2 7 PL spectra of the n.i.d. sample M400 at $T = 77$ K 40

5.3 PL of the n.i.d. sample M400 at $T = 77$ K and with different excitation intensities. 41

5.4 PL and PLE spectra of the n.i.d. sample M559 at $T = 4.2$ K. 42

6.1 Decomposition of the polarizations s_x and p_{yz} of the IR beam into the sample directions x, y and z. 45

6.2 Photo-induced intraband absorption the sample M400 (zigzag) at $T = 77$ K under different excitation intensities. 46

6.3 Infrared transmission of the sample M400 (background). 47

6.4 Decomposition of the polarizations s_y and p_{xz} of the IR beam into the sample directions x, y and z. 48

6.5 Infrared absorption of the sample M400. 49

6.6 Photo-induced intraband absorption of the sample M400 in normal incidence configuration at $T = 77$ K and $T = 300$ K. 50

6.7 Intraband absorption of the n-doped sample M499. 51

6.8 Polarization-angle dependence of the integrated infrared absorption of the n-doped sample M499. 54

6.9 Intraband absorption at normal-incidence of the doped samples M499 and M586 at $T = 300$ K. 55

6.10 Spontaneous emission of the n.i.d. sample M559. 56

6.11 Experimental setup for the infrared spontaneous emission experiment. 57

Chapter 1

Introduction

Intraband transitions, which occur between confined quantum states or bound-to-continuum states either in the valence band or in the conduction band, are specific of quantum semiconductor structures. The quantum confinement of the carriers enhances the interaction between energy levels leading to intraband transitions with a narrow bandwidth (typically $4 - 10$ meV in quantum wells and 0.1 meV in quantum dots) along with a large oscillator strength. The resonance wavelength, which depends on both physical (effective masses) and structural (size, composition) parameters of the quantum structure, exhibits a large range of tunability from near-infrared to far-infrared.

Intraband optical transitions were first observed in the 2D electron gas formed in Si inversion layers [Kam74]. Further evidences of intraband transitions were obtained in GaAs / AlGaAs heterostructures [Abs79] and quantum wells [Pin79] using resonant Raman scattering techniques. The first direct observation of IR absorption between conduction subbands of n-doped GaAs / AlGaAs quantum wells was reported in 1985 [Wes85]. It was confirmed that intersubband transitions between electronic states of quantum wells are strongly polarized along the confinement potential direction. The polarization selection rule, which states that light must have a polarization component perpendicular to the quantum well layers, has strong consequences for practical applications since normal-incidence absorption is usually forbidden. This imposes strong limitation for the fabrication of infrared photodetectors which rely on intraband absorption. Quantum wire and quantum dot systems are very attractive for these applications since normal-incidence absorption is possible there, provided that large quantum efficiencies can be achieved.

In the past two decades, the fabrication of quantum dots has been attempted using patterning, etching, layer fluctuations and collodial techniques. However, a breakthrough occured recently through the employment of self-ordering mechanisms during epitaxy of lattice-mismatched ma-

terials for the creation of high-density arrays of quantum dots that exhibit excellent optical properties. Infrared detector applications with these systems seem therefore promising, but are just beginning to be explored.

Intraband spectroscopy with a Fourier transform infrared (FTIR) spectrometer is a sound technique to explore quantum structures, because a direct measurement of the confinement energies and of the spatial symmetry of the excited states envelope wavefunctions is possible with it.

Until now, many studies on self-assembled quantum dots have been done with the InAs / GaAs material system. However, strong in-plane polarized intraband absorption has not been detected in this system up to now [Sau97]. The transitions in this system present a relatively low oscillator strength, which is due to the fact that they take place in the valence band. Additionally, the dot surface density is not yet high enough to observe strong absorption.

During this Diplomarbeit, self-assembled quantum dots of the relatively new InAs / $In_{0.52}Al_{0.48}As$ / InP system have been studied. This system features elongated and aligned quantum dots with very high surface densities.

The samples have been explored by means of atomic force microscopy (AFM), phololuminescence (PL) spectroscopy, photoluminescence excitation (PLE) spectroscopy and intraband spectroscopy.

A giant in-plane polarized absorption in the conduction band has been evidenced in the InAs / $In_{0.52}Al_{0.48}As$ / InP quantum dots. This makes this material system very promising for future infrared photodetector applications.

This Diplomarbeit is structured as follows:

- Chapter two gives a general introduction into the electronic and optical properties of semiconductor structures of different dimensions.
- The third chapter describes the Stranski-Krastanov growth process of the examined InAs / $In_{0.52}Al_{0.48}As$ / InP samples. An AFM image of a typical sample is presented and discussed.
- The experimental setup of the different methods, which were used to explore the samples, is presented in the fourth chapter. The principle of a Fourier transformation infrared (FTIR) spectrometer is also described.
- The results of the PL and PLE experiments are presented in the fifth chapter. The influence of the dot size distribution on the spectra is examined as well as their dependence on excitation intensity.

- The sixth chapter presents the intraband spectroscopy experiments. Photo-induced measurements on undoped samples as well as absorption measurements on doped samples permit to identify a strong in-plane polarized intraband absorption in the conduction band. The influence of temperature, doping density and polarization angle is studied. Preliminary experiments aiming to demonstrate the existence of intraband emission of the quantum dots are presented at last.
- Finally, chapter seven gives a conclusion of the results of this Diplomarbeit and an outlook for future experiments.

Chapter 2

Theory

In this chapter a general introduction into the electronic and optical properties of semiconductors will be given. First a 3-dimensional (3D) volume is considered, followed by the lower dimensional structures and their quantum properties. The case of a quantum well (2D) will be first treated, because the principle of heterostructure properties can be explained with it. Quantum wire (1D) and quantum dot (0D) properties will then be derived in a similar way.

2.1 Wavefunction in quantum structures

2.1.1 3D bulk material

In a 3-dimensional crystal the movement of carriers (electrons, heavy holes or light holes) near to the band edge can be described as the motion of a quasi free particle, whose effective mass m^* takes into account the interaction with the periodical lattice potential. In first approximation m^* does not depend on the direction and a continuous energy spectrum of eigenvalues, which are isotropically distributed in the $\vec{k}$-space, is obtained:

$$E^{3\mathrm{D}}(\vec{k}) = \frac{\hbar^2}{2m^*}(k_x^2 + k_y^2 + k_z^2), \tag{2.1}$$

where k_x, k_y, k_z are the wavevectors along the x, y and z-axis.

If the carriers are confined in lower dimensional systems such as 2-dimensional wells or 1-dimensional wires or 0D quantum dots with sizes of the order of the de Broglie wavelength of the carriers, a quantum structure in the electronic properties, for example the density of states, appears.

2.1.2 2D quantum well

Finite barrier

Figure 2.1 shows the bandstructure of an InAs / $In_{0.52}Al_{0.48}As$ quantum well. Electrons and holes are trapped in the one dimensional well, but can still move freely in the InAs layer. If the thickness of the active layer is of the order of the de Broglie wavelength of the carriers $\lambda_{\mathrm{Broglie}} = \frac{h}{p}$ (p being the momentum of the carrier and h the Planck constant), quantum effects will appear, i.e., the quantization of the kinetic energy in the growth direction leads to discrete energy levels in the k_z direction in both the conduction band and the valence band.

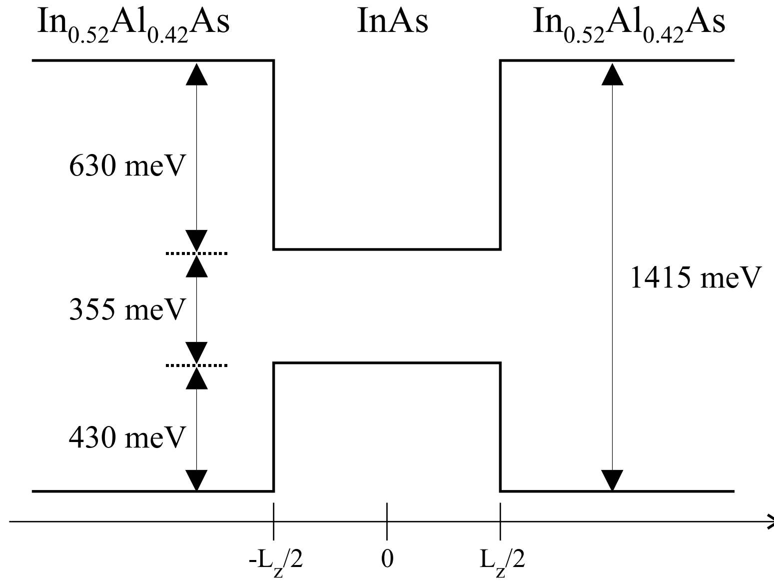

Figure 2.1: Scheme of the band structure of InAs / $In_{0.52}Al_{0.48}As$.

The calculation of the eigenenergies in the confined structure using the effective mass approximation is now illustrated. Let's assume an idealized square, finite and symmetrical potential well with a thickness L_z and a potential energy

$$V_{\mathrm{well}}(z) = \begin{cases} 0 & |z| > \frac{L_z}{2} \\ -V_{\mathrm{well}} & |z| \leq \frac{L_z}{2}. \end{cases} \tag{2.2}$$

The Schrödinger equation is:

$$\left[-\frac{\hbar^2}{2m} \triangle + V_{\mathrm{lattice}}(\vec{r}) + V_{\mathrm{well}}(z) \right] \Psi_{\mathrm{tot}}(\vec{k}, \vec{r}) = E(\vec{k}) \Psi_{\mathrm{tot}}(\vec{k}, \vec{r}), \tag{2.3}$$

where V_{lattice} is the periodical, rapidly oscillating lattice potential, which describes the interaction of the carriers with the crystal lattice. Since it oscillates on a much smaller scale than the well potential V_{well}, it can be separated. This leads to the following wavefunction:

$$\Psi_{\text{tot}}(\vec{k},\vec{r}) = \Psi_{\text{env}}(\vec{k},\vec{r}) \cdot \Phi_{\text{Bl}}(\vec{k},\vec{r}). \tag{2.4}$$

The rapidly oscillating Bloch function Φ_{Bl} represents the carrier motion in the lattice potential, which can be handled with the introduction of an effective mass m^*. Ψ_{env} is the envelope function of the Bloch function and is determined by the slowly varying potential $V_{\text{well}}(z)$. Because $V_{\text{well}}(z)$ does not contain any terms in x or y, a second separation can be carried out:

$$\Psi_{\text{env}}(\vec{k},\vec{r}) = \Phi(\vec{k}_{x,y},\vec{r}_{x,y}) \cdot \Theta(k_z, z), \tag{2.5}$$

where $\Phi(\vec{k}_{x,y},\vec{r}_{x,y})$ describes the motion in the 2 dimensions of the quantum well and leads to the energy eigenvalues:

$$E(\vec{k}_{x,y}) = \frac{\hbar^2}{2m^*_{x,y}}(k_x^2 + k_y^2), \tag{2.6}$$

with the effective mass $m^*_{x,y}$ for a motion in the layer plane.

In the z-direction a one dimensional Schrödinger equation for the motion of a free carrier with mass m^*_z in a symmetric quantum well $V_{\text{well}}(z)$ has to be solved:

$$\left[-\frac{\hbar^2}{2m^*_z}\frac{\partial^2}{\partial z^2} + V_{\text{well}}(z)\right]\Theta(k_z,z) = E_z\Theta(k_z,z). \tag{2.7}$$

The following boundary conditions must be fulfilled:

1. $\Theta(k_z, z)$ is continuous everywhere;
2. by integrating equation (2.7) around any z_0, and for the specific potential of the square quantum well, $\frac{1}{m^*_z}\frac{\mathrm{d}\Theta}{\mathrm{d}z}$ is continuous everywhere;
3. $\lim_{z\to\pm\infty} |\Theta(k_z, z)| = 0$.

The second condition accounts for the discontinuity of m^*_z at the boundary layers.

The solution of the Schrödinger equation is in this case:

$$\Theta(k_z,z) = \begin{cases} A\sin\left(\sqrt{\frac{2m^*_z E_{z,n_z}}{\hbar^2}}z - n_z\frac{\pi}{2}\right) & |z| \le \frac{L_z}{2},\ n_z = 1,2,3\dots \\ B\exp\left(-\sqrt{\frac{2m^*_{z,\text{barrier}}(V_{\text{well}}-E_{z,n_z})}{\hbar^2}}|z|\right) & |z| > \frac{L_z}{2}, \end{cases} \tag{2.8}$$

with m_z^* and $m_{z,\text{barrier}}^*$ being the effective masses in z-direction inside the quantum well and inside the barrier, respectively.

In the barrier the wavefunction is exponentially attenuated while it oscillates in the quantum well. The ground state ($n_z = 1$) is an even function and the higher states are alternately of even or odd parity.

The boundary conditions lead to a transcendental equation for the discrete energy levels E_{z,n_z} in k_z-direction, which can be solved numerically:

$$\tan\left(\sqrt{\frac{2m_z^* E_{z,n_z}}{\hbar^2}}\frac{L_z}{2} - n_z\frac{\pi}{2}\right) = -\sqrt{\frac{m_{z,\text{barrier}}^*}{m_z^*}\frac{E_{z,n_z}}{V_{\text{well}} - E_{z,n_z}}}. \tag{2.9}$$

In general, it is not possible to calculate analytically the discrete energy levels E_{z,n_z}. In order to continue these analytical calculations, an infinite barrier is assumed from now on.

Infinite barrier

For an infinite barrier height ($V_{\text{well}} \to \infty$) it is possible to get an analytical expression of the eigenenergies. The right hand side of equation (2.9) disappears and the energy eigenvalues are:

$$E_{z,n_z} = \frac{\hbar^2\pi^2}{2m_z^*}\left(\frac{n_z^2}{L_z^2}\right). \tag{2.10}$$

The total energy of the two dimensional system is then given by:

$$\begin{aligned} E_{n_z}^{2\text{D}}(k_x, k_y) &= E_{z,n_z} + E(\vec{k}_{x,y}) = E_{z,n_z} + \frac{\hbar^2}{2m_{x,y}^*}\left(k_x^2 + k_y^2\right) \\ &\overset{V_{\text{well}}\to\infty}{=} \frac{\hbar^2\pi^2}{2m_z^*}\left(\frac{n_z^2}{L_z^2}\right) + \frac{\hbar^2}{2m_{x,y}^*}\left(k_x^2 + k_y^2\right). \end{aligned} \tag{2.11}$$

This energy function is the sum of discrete and continuous energy eigenvalues. The continuous energy band $E \propto \vec{k}^2$ of the 3D case splits up in several subbands which are determined by the quantum number n_z. The lowest energy level in the quantum well has shifted to a value greater than zero, because $n_z \geq 1$. There is always at least one bound energy level in the k_z direction of a quantum well with infinite barriers, even if its thickness L_z is very small.

Non-parabolicity

Equation (2.11) is only valid if the conduction and valence bands are parabolic. The real band scheme in a semiconductor is different from this ideal model and the actual energy levels are

shifted with respect to the levels calculated by the parabolic band model. The dispersion relation $E(\vec{k}_{x,y}) \propto \vec{k}_{x,y}^2$ is only valid, if $\vec{k}_{x,y} \to 0$. As $\vec{k}_{x,y}$ increases, the value of the effective mass increases also.

To solve this problem, Kane has proposed a model for small bandgap semiconductors [Kan75], which takes into account the interaction of the different bands. By retaining solely terms up to the second order, the dispersion relation of the conduction band can be written as [Vag94]:

$$E_{n_z}^{2D}(\vec{k}_{x,y}) = E_{z,n_z} + \frac{\hbar^2 \vec{k}_{x,y}^2}{2m^*} + \frac{\alpha}{E_g}\left(\frac{\hbar^2 \vec{k}_{x,y}^2}{2m^*}\right)^2, \tag{2.12}$$

where the non-parabolicity coefficient α is defined as

$$\alpha = -\frac{(1 - \frac{m^*}{m_0})^2(3E_g^2 + 4E_g\Delta_{so} + 2\Delta_{so}^2)}{(E_g + \Delta_{so})(3E_g + 2\Delta_{so})}. \tag{2.13}$$

E_g is the bandgap energy and Δ_{so} the spin-orbit coupling.

Equation (2.12) can be expressed using an energy dependent effective mass:

$$E_{n_z}^{2D}(\vec{k}_{x,y}) = E_{z,n_z} + \frac{\hbar^2 \vec{k}_{x,y}^2}{2m^*(E)}, \tag{2.14}$$

with

$$m^*(E) = \frac{m^*}{1 + \sqrt{4\alpha \frac{E - E_{z,n_z}}{E_g}}}. \tag{2.15}$$

Similar relations describe the valence band of the light holes. The heavy holes in the valence band, however, generally do not need a non-parabolicity treatment, as their big effective mass implies, for a given energy, a high density of states.

Strain

In heterostructures, where the lattice constants of the quantum well material and the barrier material are not the same, the electronic properties change with respect to the simple model developed above. In fact, the lattice constant in the layer plane of the deposited material will be adapted to that of the substrate (see section 3.1). This adaptation is compensated by a tetragonal deformation of the unit cell which leads to a reduction (for layers in tension) or to an increase (for layers in compression) of the lattice constant perpendicular to the layer plane. This causes

the presence of strain at the interface of the two materials. The presence of strain in the layers does not only modify the energy of the bandgap, but also the effective masses of the carriers, which become strongly anisotropic.

In the example of figure 2.2 a material with lattice constant a, which is higher (lower) than the constant of the substrate a_s, is grown onto the substrate. When the two layers get in contact with each other, a compression (tension) strain is imposed to the layer. This biaxial strain causes a lifting of the degeneracy in the valence band at $k = 0$ as shown in figure 2.2. The material in tension (compression) strain has a lower (higher) bandgap than a relaxed material of the same composition.

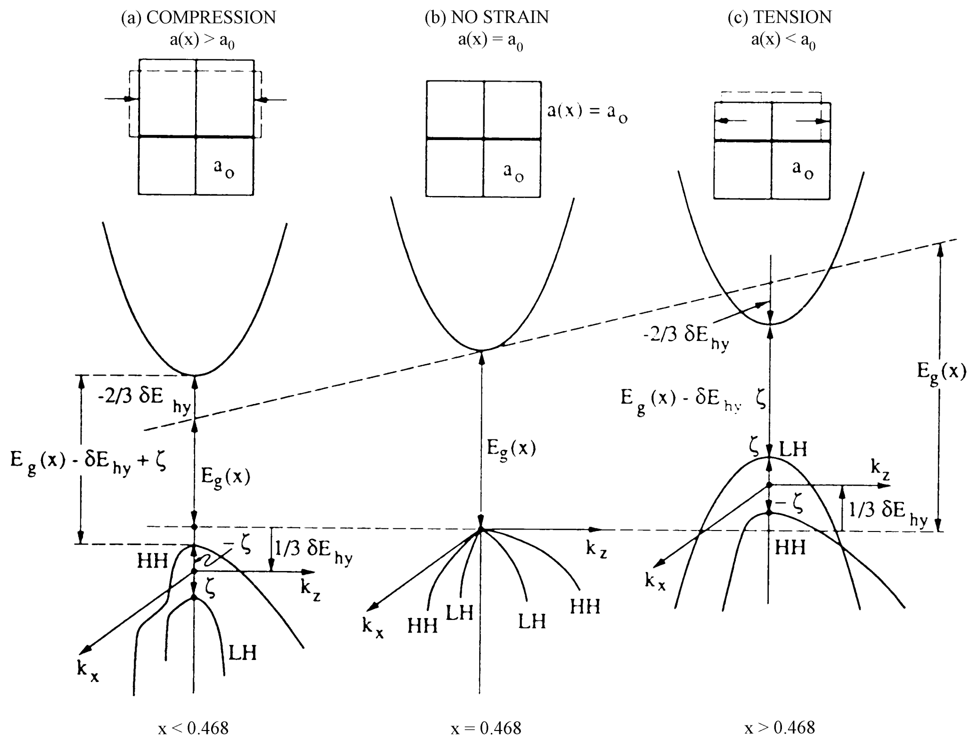

Figure 2.2: Effects of biaxial strain: decrease of the degeneracy of the valence band and change of the effective masses in the $Ga_xIn_{1-x}As$ / $Ga_xIn_{1-x}As_yP_{1-y}$ *material system (from [Chu91]).*

The biaxial strain in the layer plane due to lattice mismatch is [Fra94]:

$$\varepsilon_{xx} = \varepsilon_{yy} = \frac{a - a_s}{a_s}, \tag{2.16}$$

and in the growth direction:

$$\varepsilon_{zz} = -2\frac{C_{12}}{C_{11}}\varepsilon_{xx}, \tag{2.17}$$

where C_{ij} are the material elastic constants.

For a biaxial strain, the difference of the energies at the bottom of the conduction band and the subbands in the valence band is in first approximation given by:

$$\Delta E_0(e-hh) = \left[-2a\left(\frac{C_{11}-C_{12}}{C_{11}}\right) + b\left(\frac{C_{11}+2C_{12}}{C_{11}}\right)\right]\frac{\Delta a}{a}, \tag{2.18}$$

$$\Delta E_0(e-lh) = \left[-2a\left(\frac{C_{11}-C_{12}}{C_{11}}\right) - b\left(\frac{C_{11}+2C_{12}}{C_{11}}\right)\right]\frac{\Delta a}{a}, \tag{2.19}$$

where $\Delta E_0(e-hh)$, $\Delta E_0(e-lh)$ are the energy variations of the conduction band–heavy holes and conduction band–light holes transitions respectively. a and b are the conduction band and valence band deformation potentials.

Figure 2.2 has been calculated for $Ga_xIn_{1-x}As$ grown on a $Ga_xIn_{1-x}As_yP_{1-y}$ lattice matched to InP [Chu91]. The dotted line represents the bandgap of the relaxed material (which depends on the composition x of the $Ga_xIn_{1-x}As$ layer). δE_{hy} and ζ represent the first and second term of equation (2.19), respectively. As the parameters of the InAs / $In_{0.52}Al_{0.48}As$ system, which has been examined during this Diplomarbeit, are close (appendix A) to those used in figure 2.2, the influence of biaxial strain for InAs will be similar.

2.1.3 1D quantum wire

If the motion of the carriers is confined in further directions of space, the additional quantization can be calculated in a way analogous to that of the quantum well. For a one dimensional system (quantum wire) with infinite barriers the energy eigenvalues are:

$$E^{1D}_{n_x,n_z}(k_y) = \frac{\hbar^2\pi^2}{2}\left(\frac{n_x^2}{m_x^* L_x^2} + \frac{n_z^2}{m_z^* L_z^2}\right) + \frac{\hbar^2 k_y^2}{2m_y^*}. \tag{2.20}$$

The energy function is again a sum of discrete and continuous eigenvalues, which leads to an unidimensional subband structure.

2.1.4 0D quantum dot

For a parallelepipedic quantum dot one obtains:

$$E^{0D}_{n_x,n_y,n_z} = \frac{\hbar^2\pi^2}{2}\left(\frac{n_x^2}{m_x^* L_x^2} + \frac{n_y^2}{m_y^* L_y^2} + \frac{n_z^2}{m_z^* L_z^2}\right), \tag{2.21}$$

where $(n_x, n_y, n_z) \in (\mathbf{N}^3)^*$ are the quantum numbers. They are integers, but not all of them are allowed to be 0. $L_{x,y,z}$ are the sizes of the structure and $m^*_{x,y,z}$ the effective masses in the respective directions.

The carriers in a quantum dot are completely localized and only discrete energy levels exist.

In the realistic case of finite potential wells, numerical calculations must be performed to find an exact solution of the Schrödinger equation.

In real situations, such as self organized quantum dots, exact calculations of the discrete energy levels proved to be very difficult and have only been performed numerically for the InAs / GaAs quantum dot system [Mar94, Gru95, Zun98]. First, the exact shape of the dot is usually not known (facets of pyramids, radii in lens shape, ...). Second, anisotropic strain largely influences the electronic properties of 1D and 0D quantum structures.

Strain

Figure 2.3 shows as an example the strain distribution for an InAs / GaAs quantum dot, which has the shape of a square pyramid. Far away form the dot in the wetting layer there is biaxial strain which is entirely confined in the wetting layer: because InAs has a smaller lattice constant than GaAs, in x and y direction the InAs layer is compressed (ε_{xx} and ε_{yy} are negative) and in the z direction a tension strain can be distinguished ($\varepsilon_{zz} > 0$). The strain distribution inside the pyramid is different. Close to the lower interface, ε_{zz} is still positive but much smaller than in the wetting layer because the substrate can no longer force the interface lattice constant to be that of the substrate. With increasing height within the dot, ε_{zz} changes its sign and becomes negative at the top of the pyramid. This happens because at the very top only small forces act on the quantum dot in the xy plane, but the GaAs barrier compresses the pyramid mainly from the sides along the z direction, imposing tensile strain components in the xy plane ($\varepsilon_{xx} = \varepsilon_{yy}$ become positive). Generally, however, the strain is still compressive even at the top of the pyramid ($\mathrm{Tr}\varepsilon < 0$) [Gru95]. Around the pyramid the barrier also becomes significantly strained.

Because the strain distribution and the exact shape of the dots have to be known, calculating the correct electronic structure is difficult. Most approaches have been done using a $\vec{k} \cdot \vec{p}$ model (where $\vec{k}$ is the wave vector and $\vec{p}$ is the momentum) [Cus96, Cus97]. It calculates the $E(\vec{k})$ relationship over a small k range around the band extrema for multiple bands. Another approach considers the dot as a structure in its own right (rather than viewing it as a perturbation of the bulk material)[Zun98]. The model is based on a pseudopotential framework and uses no adjustable parameters outside the bulk band structure. Figure 2.4 shows the electron and hole wavefunction for the ground state and excited states for a self assembled InAs / GaAs system calculated with the pseudopotential framework. As expected the ground electron state wave-

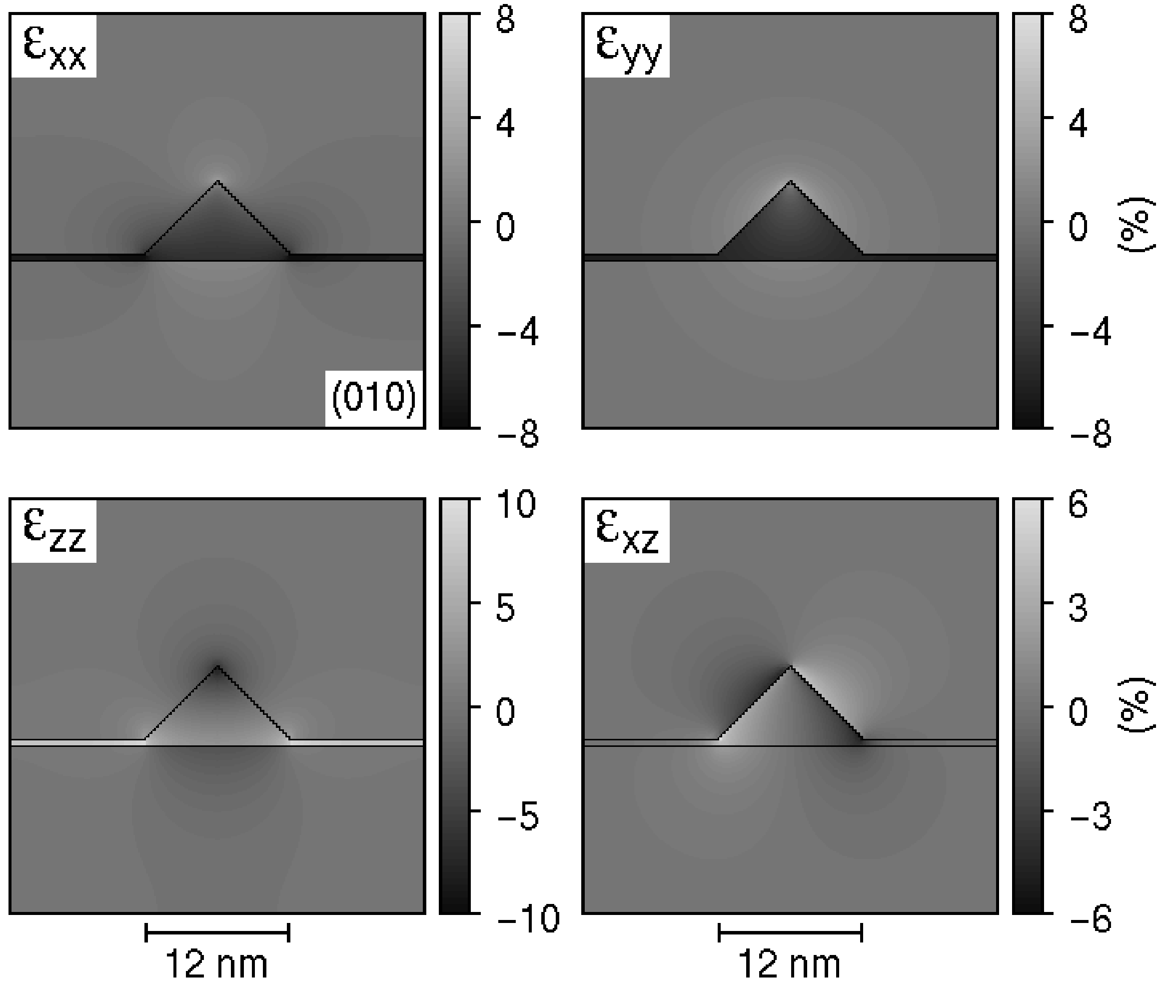

Figure 2.3: Strain distribution in the (010) plane through the top of the pyramid of an InAs *quantum dot grown on* GaAs *[Gru95].*

function lays almost completely within the dot and covers a large part of it. However, excited states represent nodes with different shapes localized at the corners of the pyramid. Hence, the small dimensions of the dot and the presence of anisotropic strain have large effects on the form of the wavefunctions.

Although the two aproaches give a fair description of the hole and electron wavefunctions, the models strongly differ on the energetic structure of the dots especially for the excited states. They also do not account for the depletion of the wetting layer around the pyramids. No calculations have yet been performed for our InAs / $In_{0.52}Al_{0.48}As$ quantum dot system.

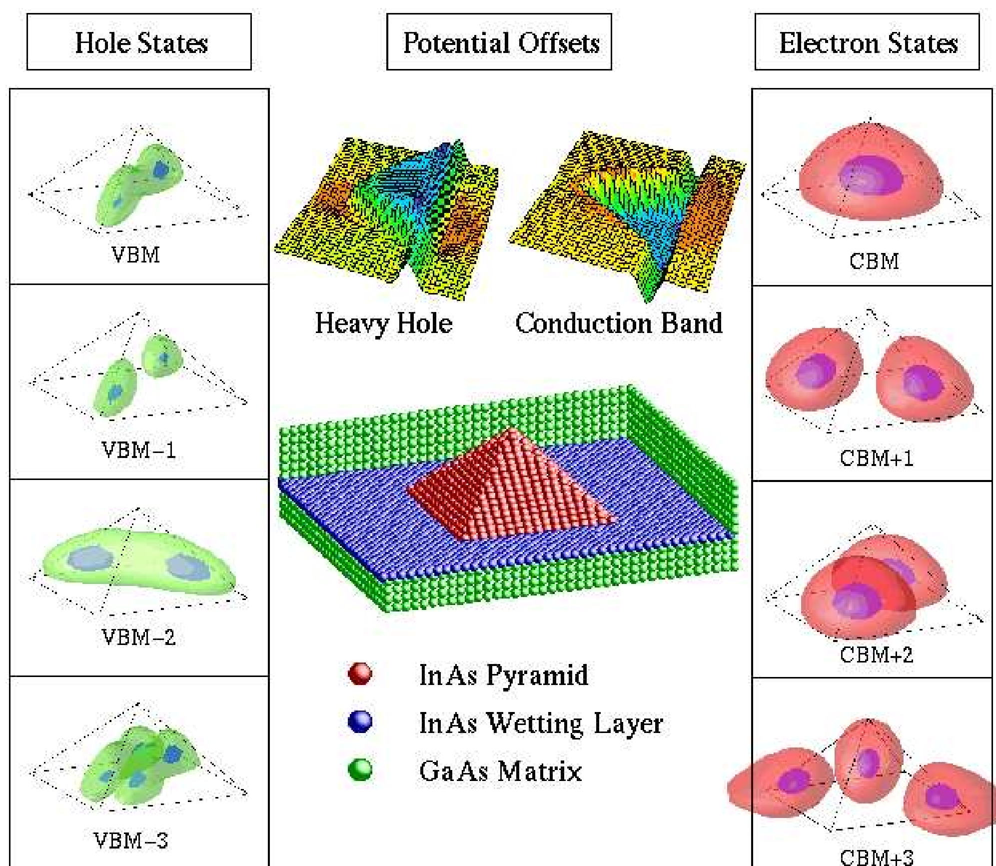

Figure 2.4: The electronic structure of a strained InAs (110) pyramidal quantum dot embedded within GaAs. The strain-modified band offsets are shown above the atomic structure. They exhibit a well for both heavy holes and electrons. Isosurface plots of the four highest hole states and four lowest electron states, as obtained from pseudopotential calculations, appear on the left and right. CBM means conduction band minimum and VBM valence band minimum (from [Zun98]).

2.2 Density of states

As seen in the previous section, the energy dependence in $\vec{k}$-space changes when the dimension of free particle motion is decreased. This is why the density of states $\rho(\epsilon)$ is expected to change as well. In the case of infinite barriers $\rho(\epsilon)$ can be evaluated for the systems of different dimensions using the definition

$$\rho(\epsilon) = 2 \sum_{n,k} \delta\left(\epsilon - E_n(\vec{k})\right), \tag{2.22}$$

which takes the spin degeneracy into account and where δ represents the Dirac function and $E_n(\vec{k})$ the energy eigenvalues for the different systems (equations (2.1),(2.11),(2.20) and (2.21)).

The following energy dependences of the density of states are obtained [Ara82]:

$$\begin{aligned}
\rho^{3\mathrm{D}}(\epsilon) &\propto \sqrt{\epsilon}, \\
\rho^{2\mathrm{D}}(\epsilon) &\propto \sum_{n_z} H(\epsilon - E_{n_z}), \\
\rho^{1\mathrm{D}}(\epsilon) &\propto \sum_{n_x,n_z} \frac{1}{\sqrt{\epsilon - E_{n_x} - E_{n_z}}}, \\
\rho^{0\mathrm{D}}(\epsilon) &\propto \sum_{n_x,n_y,n_z} \delta(\epsilon - E_{n_x} - E_{n_y} - E_{n_z}),
\end{aligned} \tag{2.23}$$

with H being the Heavyside function.

Figure 2.5 shows a schematic representation of the density of states for 3D, 2D, 1D and 0D systems. In the 3-dimensional case a quasicontinuous distribution of the energy eigenlevels is obtained. The density of states increases with the root of the energy.

For a quantum well, the lowest energy level is, respective to the 3D case, shifted to higher energies by the quantization energy of the first 2D subband. This means that the density of states is zero for energies smaller than those at the beginning of the first subband. If the first subband is reached, the density of states jumps up to a constant value, which is maintained until the next subband is reached. The result is a staircase like energy dependence of $\rho^{2\mathrm{D}}(\epsilon)$.

For a quantum wire, the density of states also jumps up if a new subband of higher energy is reached, but it decreases for increasing energies following an $\epsilon^{-\frac{1}{2}}$ proportionality, until the next subband is reached.

In a quantum dot only discrete energy levels exist, and therefore the density of states is a sum of δ-functions. Only two electrons with spins up and down, respectively, can populate each level.

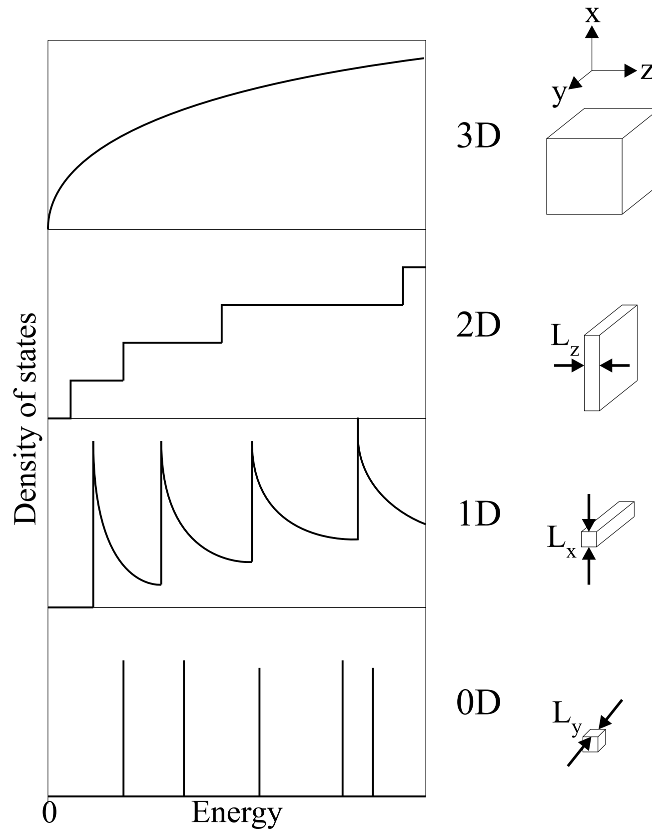

Figure 2.5: Schematic representation of the energy dependence of the density of states for 3D, 2D, 1D and 0D systems.

2.3 Optical transitions

In this section, the main optical properties of low dimensional structures are discussed. The case of a single quantum well is firstly considered and lower dimensional structures are then treated in a similar way.

Two kinds of optical transitions are considered (figure 2.6). *Interband* transitions take place between the conduction band and the valence band and involve two kinds of carriers (they are *bipolar*), electrons and holes. The energy of the transition is the bandgap energy plus the confinement energies of the electrons and holes minus the exciton binding energy. *Intraband* transitions happen inside either the conduction or the valence band and involve only one type of carrier (the transition is *unipolar*). In a quantum dot, intraband transitions occur between discrete energy levels. In quantum wells and quantum wires there exist subbands inside the conduction or the valence band. Intraband transitions in these structures between two subbands are called *intersubband* transitions. Note that another type of intraband transitions may occur which involves the transitions of a carrier from one subband to the same subband with absorp-

tion of a photon and emission of a phonon (momentum conservation). The latter is the analogue of free carrier absorption.

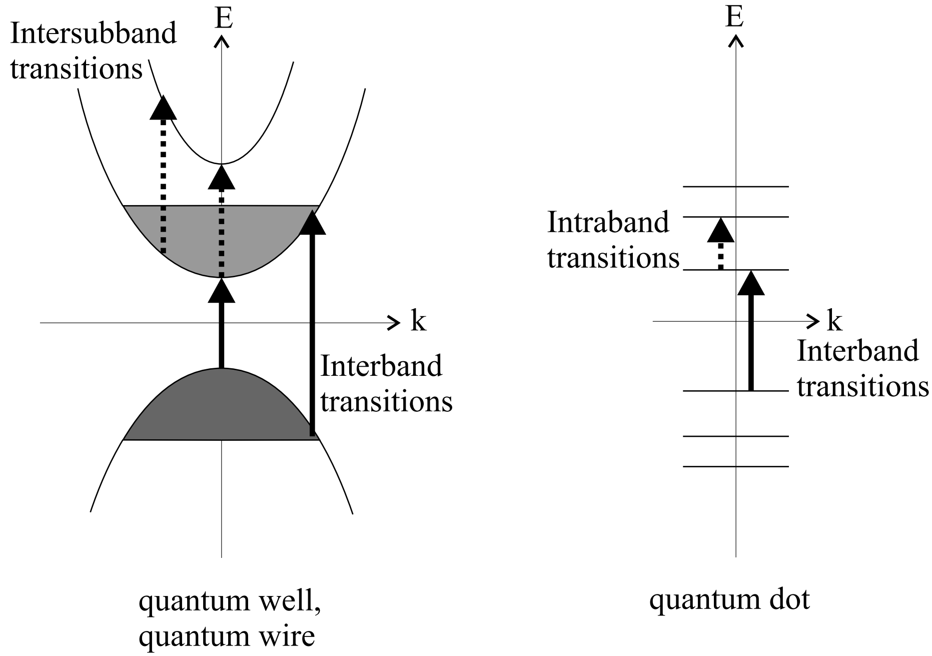

Figure 2.6: Interband and intraband transitions for quantum wells, quantum wires (left) and quantum dots (right). The diagrams show a scheme of the band/level structure.

To describe the optical properties of several material systems, the absorption coefficient in a quantum well or a quantum wire is first discussed in the electric dipole approximation [Mou96, Bas88].

The electrical field of a light wave with frequency ω and wavevector $\vec{k}$ ($|k| = \frac{n\omega}{c}$) can be expressed as

$$\vec{F}(\vec{r}, t) = F\vec{\varepsilon}\cos(\omega t - \vec{k} \cdot \vec{r}), \tag{2.24}$$

with $\vec{\varepsilon}$ being a supposed linear polarization. In the Coulomb gauge ($\text{div}\vec{A} = 0$), the electrical field depends on the vector potential $\vec{A}$ as follows:

$$\vec{F} = -\frac{1}{c}\frac{\partial \vec{A}}{\partial t}. \tag{2.25}$$

This leads to

$$\vec{A}(\vec{r}, t) = -\frac{\vec{\varepsilon}cF}{2i\omega}\left[\exp\left(i(\omega t - \vec{k} \cdot \vec{r})\right) - \exp\left(-i(\omega t - \vec{k} \cdot \vec{r})\right)\right]. \tag{2.26}$$

The one electron Hamiltonian of a heterostructure in presence of an electromagnetic field is in first approximation:

$$H = H_0 + \frac{e}{2m_0 c}\left(\vec{p}\cdot\vec{A} + \vec{A}\cdot\vec{p}\right), \tag{2.27}$$

with the electron momentum $\vec{p}$ and the electron charge e.

The probability of an optical stimulated transition is given by Fermi's golden rule:

$$\tilde{P}_{if} = \frac{2\pi}{\hbar}|\langle f|V|i\rangle|^2 \cdot \delta(\epsilon_f - \epsilon_i - \hbar\omega), \tag{2.28}$$

where V is the perturbation term of the Hamiltonian $H = H_0 + V$. Under the electric dipole approximation ($\exp(-i\vec{k}\cdot\vec{r}) \approx 1$), which is valid for visible and infrared wavelengths, V is:

$$V = \frac{ieF}{2m_0\omega}\vec{\varepsilon}\cdot\vec{p}. \tag{2.29}$$

If the quantum states i and f are partially occupied, the transition probability has to be weighted by the occupancy factor given by the Fermi distribution $f(\epsilon)$:

$$P_{if} = \tilde{P}_{if} f(\epsilon_i)[1 - f(\epsilon_f)], \tag{2.30}$$

where the Fermi distribution is the mean occupancy of the state ν:

$$f(\epsilon_\nu) = \left[1 + \exp\left(\frac{1}{k_B T}(\epsilon_\nu - \mu)\right)\right]^{-1}. \tag{2.31}$$

When taking into account the transitions $i \to f$ and $f \to i$, the linear absorption coefficient is given by:

$$\alpha(\omega) = A\sum_{i,f}\frac{1}{m_0^*}|\vec{\varepsilon}\cdot\vec{p}_{if}|^2\delta(\epsilon_f - \epsilon_i - \hbar\omega)\left[f(\epsilon_i) - f(\epsilon_f)\right], \tag{2.32}$$

with $\vec{p}_{if} = \langle i|\vec{p}|f\rangle$, which contains the selection rules information, and $A = \frac{4\pi^2 e^2}{ncm_0\omega\Omega}$. $\Omega = SL$ is the irradiated volume of the sample.

2.3.1 Dipole moment and selection rules

Quantum well

In the case of a quantum well (QW), the wavefunction of a state i is given by (equation (2.4), (2.5) and [Bas88]):

$$\Psi_i(\vec{r}) = \Phi_{\mathrm{Bl},i}(\vec{r})\Psi_{\mathrm{env},i}(\vec{r}) = \Phi_{\mathrm{Bl},i}(\vec{r})\frac{1}{\sqrt{S}}\exp(i\vec{k}_{x,y}\cdot\vec{r}_{x,y})\Theta_i(z), \tag{2.33}$$

where $\Phi_{\mathrm{Bl},i}(\vec{r})$ is the periodic part of the Bloch function at the band extremum, $\vec{k}_{x,y}$ and $\vec{r}_{x,y}$ are the wave and position vectors in the quantum well layer plane, $\Theta_i(z)$ is the envelope function for subband i in the z confinement direction and S is the area. Accounting for the rapid variations of the Bloch functions over $\frac{1}{k_{x,y}}$ and over the spatial extent of the envelope wave functions

$$\vec{\varepsilon}\cdot\vec{p}_{if} \approx \vec{\varepsilon}\langle\Phi_{\mathrm{Bl},i}|\vec{p}|\Phi_{\mathrm{Bl},f}\rangle\langle\Psi_{\mathrm{env},i}|\Psi_{\mathrm{env},f}\rangle + \langle\Phi_{\mathrm{Bl},i}|\Phi_{\mathrm{Bl},f}\rangle\langle\Psi_{\mathrm{env},i}|\vec{\varepsilon}\cdot\vec{p}|\Psi_{\mathrm{env},f}\rangle \tag{2.34}$$

is obtained. The first term on the right-hand side is the optical matrix element for interband transitions which gives rise to the band-to-band selection rules. The second term is the intersubband contribution, since by definition the Bloch functions are identical for both subbands ($\langle\Phi_{\mathrm{Bl},i}|\Phi_{\mathrm{Bl},f}\rangle = \delta_{if}$ and $\langle\Phi_{\mathrm{Bl},i}|\vec{p}|\Phi_{\mathrm{Bl},f}\rangle = 0$). The intersubband optical matrix element is equal to

$$\langle\Psi_{\mathrm{env},i}(\vec{r})|\vec{\varepsilon}\cdot\vec{p}|\Psi_{\mathrm{env},f}(\vec{r})\rangle = \frac{i(\epsilon_f-\epsilon_i)m_0}{\hbar e}\mu_{if} \tag{2.35}$$

with the intersubband dipole moment

$$\mu_{if} = e\langle\Theta_i(z)|z|\Theta_f(z)\rangle\vec{\varepsilon}\cdot\hat{z}. \tag{2.36}$$

$\hat{z}$ is the unit vector in the z direction, ϵ_ν is the confinement energy and m_0 the free electron mass. As seen, the dipole moment only involves the envelope wave functions for the two subbands. In symmetric QWs, since z is odd, only transitions between subbands with opposite parity of the envelope wave functions are allowed: $f-i=\pm1,\pm3,\ldots$.

For example, transitions from the ground state to the first excited state are allowed but transitions from the ground state to the second excited state are forbidden. This selection rule is, of course, not relevant for asymmetric potential profiles, such as step QWs or DC-biased QWs, for which all transitions become allowed. The dipole moment is polarized normally to the layer plane, i.e., along the $\hat{z}$ confinement direction. Tables 2.1 and 2.2 show the selection rules for the different polarizations of interband transitions and intersubband transitions in a quantum well. Using

Table 2.1: Selection rules for interband transitions (from [Bas88]).

Polarization	ε_x	ε_y	ε_z	Type of transition
Propagation ǁ $\hat{z}$	$\Pi/\sqrt{2}$	$\Pi/\sqrt{2}$	impossible	$HH_n \to E_m$
Propagation ǁ $\hat{x}$	impossible	$\Pi/\sqrt{2}$	forbidden	$HH_n \to E_m$
Propagation ǁ $\hat{y}$	$\Pi/\sqrt{2}$	impossible	forbidden	$HH_n \to E_m$
Propagation ǁ $\hat{z}$	$\Pi/\sqrt{6}$	$\Pi/\sqrt{6}$	impossible	$LH_n \to E_m$
Propagation ǁ $\hat{x}$	impossible	$\Pi/\sqrt{6}$	$2\Pi/\sqrt{6}$	$LH_n \to E_m$
Propagation ǁ $\hat{y}$	$\Pi/\sqrt{6}$	impossible	$2\Pi/\sqrt{6}$	$LH_n \to E_m$

Table 2.2: Selection rules for intersubband transitions of a quantum well(from [Bas88]).

Polarization	ε_x	ε_y	ε_z
Propagation ǁ $\hat{z}$	forbidden if $\omega \neq 0$	forbidden if $\omega \neq 0$	impossible
Propagation ǁ $\hat{x}$	impossible	forbidden if $\omega \neq 0$	allowed
Propagation ǁ $\hat{y}$	forbidden if $\omega \neq 0$	impossible	allowed

the so-called infinite quantum well approximation, i.e., assuming an infinite barrier potential on both sides of the well, one can derive the following expression for the dipole:

$$\mu_{if} = \frac{8}{\pi^2}\frac{if}{(f^2 - i^2)^2} eL_z \sin(\theta), \tag{2.37}$$

where i and f are the subband indexes, L_z is the well's width and θ is the angle between the direction of incident light and the direction perpendicular to the layers. Therefore, for the transition between the ground state and the first excited state, the dipole for light polarized perpendicularly to the layers ($\theta = \frac{\pi}{2}$) is:

$$\mu_{12} = \frac{16}{9\pi^2} eL_z \approx 0.18 eL_z. \tag{2.38}$$

The equivalent dipole length of intersubband transitions is giant, of the order of 18 % of the well width. The simple model presented above holds very well for bound-to-bound levels intersubband transitions in the conduction band. It is clearly a gross approximation for intersubband

transitions in the valence band since the hole wave function must account for the strong coupling at $k \neq 0$ between the heavy hole, light hole and spin-orbit subbands. Normal incidence excitation of hole intersubband transitions is allowed because of this coupling [Cha89].

Quantum wire

The treatment can be extended to lower dimensional systems. In the case of a 1D confinement (quantum wire), one can show that for electronic transitions between 1D subbands there is only one forbidden direction for the polarization vector which is parallel to the wire axis (table 2.3).

Table 2.3: Selection rules for intersubband transitions of a quantum wire. The wire axis is parallel to the y direction.

Polarization	ε_x	ε_y	ε_z
Propagation $\parallel \hat{z}$	allowed	forbidden if $\omega \neq 0$	impossible
Propagation $\parallel \hat{x}$	impossible	forbidden if $\omega \neq 0$	allowed
Propagation $\parallel \hat{y}$	allowed	impossible	allowed

Quantum dot

For 0D systems, there is *a priori* no forbidden direction but the actual polarization of intraband transitions between confined levels will depend on the spatial wave function symmetry of the states involved (see section 2.1.4), since the dipole is $\mu_{if} = e\langle\Psi_i|\vec{\varepsilon}\cdot\vec{r}|\Psi_f\rangle$. This means that the polarization of the intraband dipole can be predicted by means of simple symmetry considerations. For example, the transition VBM $\rightarrow$ VBM-1 in Figure 2.4 is polarized along the growth direction, whereas VBM $\rightarrow$ VBM-2 is polarized in the wetting layer plane.

Normal incidence intraband absorption in quantum wells is usually forbidden. However, in quantum wires and quantum dots in-plane polarized transitions become possible, which is of great interest for the development of IR photodetectors irradiated at normal-incidence.

Intraband spectroscopy is a sound experimental technique for investigating low dimensional semiconductors, since one can get insight on the confinement energies and on the spacial symmetrie of the excited states, because the polarizations of the transitions can be measured.

2.3.2 Oscillator strength

The oscillator strength of an intraband transition between the ground state and the first excited state is:

$$f = \frac{2m_0 E_{21}}{e^2\hbar^2}\mu_{12}^2, \tag{2.39}$$

where E_{21} is the energy difference between the two states. The oscillator strength of intersubband transitions does not depend on the energy of the transition, i.e., on the width of the quantum well, but only depends on the carrier effective mass which is material dependent: Because the intersubband energy $E_{21} \approx 3\hbar^2\pi^2/(2m^* L_z^2)$ and because of equation (2.38), equation (2.39) simplifies to $f \approx 0.96\frac{m_0}{m^*}$, where m^* is the effective mass. Lower effective masses give larger oscillator strengths. For example, in the Γ conduction band, $f \approx 14$ in GaAs QWs ($m_c^* \approx 0.067 m_0$) and $f \approx 42$ in InAs QWs ($m_c^* \approx 0.023 m_0$). It can be shown that this giant magnitude of the oscillator strength of intersubband transitions is in fact comparable to that of interband transitions [Khu92].

2.3.3 Intraband absorption

The intraband absorption coefficient for the $1 \rightarrow 2$ transition in a quantum structure can be expressed as [Yan91]:

$$\alpha(\omega) = \frac{\pi E_{21} e^2 (n_1 - n_2)}{2\epsilon_0 c \tilde{n} m_0 \omega \Omega} \cdot f \cdot g(E_{21} - \hbar\omega), \tag{2.40}$$

where $n_1 - n_2$ is the number of carriers, which can absorb in the active volume Ω of the quantum structure, ϵ_0 the dielectrical constant and $\tilde{n}$ the refractive index. f is the oscillator strength (equation (2.39)) and $g(\omega)$ is a lineshape function.

The spectral lineshape $g(\omega)$ takes into account several contributions:

- The homogeneous spectral width due to the finite coherence time between the two levels. This width can be expressed by a Lorentzian lineshape:

$$L(\omega) = \frac{1}{\pi}\frac{\hbar\Gamma}{(E_{21} - \hbar\omega)^2 + \hbar^2\Gamma^2}, \tag{2.41}$$

  where $2\hbar\Gamma$ is the full width at half maximum (FWHM) of the intraband resonance.

- The inhomogeneous broadening caused by imperfections of the structure. In the case of a quantum well, imperfections are mainly variations of the width of the layer. For quantum

wires and dots, size distributions of the structures are the origin of this lineshape broadening. For the example of quantum dots, this can be explained as followed: Smaller dots have higher energy levels and also greater differences between two states in one 'band', while greater dots possess smaller energy differences between two states. As the absorption takes place in a huge number of quantum dots, the sum of all their narrow absoption lines at different energy positions will be observed. The result is that the absorption spectrum overtakes the shape of the size distribution function of the dots.

- The inhomogeneous spectral width introduced by the non-parabolicity or, more general, by the coupling with other levels. This causes an asymmetric lineshape [Iko89].

2.3.4 Temperature dependance

The integrated absorption of an intraband absorption peak is defined as

$$I = \int_0^\infty \frac{\Delta t(\omega)}{t(\omega)}\,\mathrm{d}\omega = \int_0^\infty \alpha(\omega) L\,\mathrm{d}\omega, \tag{2.42}$$

where $t(\omega)$ is the sample transmission, $\Delta t(\omega)$ the measured decrease of transmission due to absorption, $\alpha(\omega)$ the absorption coefficient from equation (2.40) and L the length of the IR beam path through the absorbant material. Equation (2.42) expresses the correlation between experimental data $\frac{\Delta t}{t}$ and the calculated absorbance α. I depends on the temperature of the sample through the carrier density in the initial and final state n_i and n_f:

$$I = \sigma(n_i - n_f), \tag{2.43}$$

where σ is the absorption cross section. The temperature dependence of n_i and n_f depends on the statistic which describes the energy distribution of electrons. In the case of a quantum well and quantum wire, the Fermi distribution is valid, while for the population of the discrete energy levels of a quantum dot the Gibbs distribution for the grand canonical ensemble has to be used.

Quantum wire

In a quantum wire the population $n(\varepsilon)$ of an energy level ε is determined by

$$n(\varepsilon) = \rho(\varepsilon)\frac{1}{1+\exp\left(\frac{\varepsilon-\varepsilon_\mathrm{F}}{kT}\right)}, \tag{2.44}$$

where the fraction represents the Fermi distribution with the Fermi energy ε_F, k is the Boltzmann constant and

$$\rho(\varepsilon) = 2\frac{L_y}{\pi\hbar}\sqrt{\frac{m^*}{2}}\sum_{n_x,n_z}\mathrm{Re}\left(\frac{1}{\sqrt{\varepsilon-\varepsilon_{n_x}-\varepsilon_{n_z}}}\right) \tag{2.45}$$

is the density of states of a 1D wire.

The Fermi energy ε_F can be calculated by integrating over all energies, thus by solving the equation

$$n = \int_0^\infty \rho(\varepsilon)\frac{1}{1+\exp\left(\frac{\varepsilon-\varepsilon_\mathrm{F}}{kT}\right)}\,\mathrm{d}\varepsilon. \tag{2.46}$$

n is in this case the total carrier density in the quantum wire.

This simple model allows the population of energy levels for different temperatures to be numerically calculated. By using equation (2.43), ratios of integrated absorptions at different temperatures can be calculated and compared with experimental data.

Quantum dot

Since quantum dots have only discrete energy levels (each occupied at maximum with 2 carriers with spin up and down) and a limited number of carriers is present in each dot, the Gibbs distribution in the grand canonical ensemble has to be used to describe the occupation of levels by the carriers in the dots [Bee91, Ave91]. If the occupation number of carriers in the level i is n_i (the number n_i can take on only the values 0, 1 and 2) and $\{n_i\} \equiv \{n_1, n_2, \ldots\}$ are the possible realizations of occupation numbers of the energy levels in the quantum dot, then the probability $P(\{n_i\})$ of finding the dot in the state $\{n_i\}$ is given by:

$$P(\{n_i\}) = Z^{-1}\exp\left[-\frac{1}{kT}\left(\sum_{i=1}^{\infty}\varepsilon_i n_i - N\varepsilon_\mathrm{F}\right)\right], \tag{2.47}$$

where $N \equiv \sum_i n_i$ is the total number of carriers in the dot and Z is the partition function:

$$Z = \sum_{\{n_i\}}\exp\left[-\frac{1}{kT}\left(\sum_{i=1}^{\infty}\varepsilon_i n_i - N\varepsilon_\mathrm{F}\right)\right]. \tag{2.48}$$

Intraband transitions from a level i to a level f are only possible in dots, where the level i is filled with at least one carrier ($n_i = 1, 2$) and the level f can still take up one carrier ($n_f = 0, 1$).

The probability of finding dots with these occupation conditions can be calculated for different temperatures. Since the integrated absorption is proportional to the number of dots which fullfil this condition, the absorption dependence on the temperature can be determined.

Chapter 3

Sample growth and AFM characterization

In this chapter the growth process and first characterization by atomic force microscopy (AFM) of the samples are described.

3.1 Stranski Krastanov growth

The quantum dots examined during this work were produced using a self-assembly mechanism. The deposit of a material layer with lattice constant a onto a substrate of lattice constant a_s imposes the crystal structure of the substrate to the layer. This causes elastic strain, which can relax in different ways. In a two dimensional film the lattice constant parallel to the surface will be matched to $a_{||} = a_s$ ($\Delta a = a_s - a < 0$). Perpendicular to the layer the lattice constant will be increased to $a_{\perp} = a - 2(a_s - a)\frac{\nu}{(1-\nu)}$; the result is a tetragonal distortion. ν is the Poisson number and its value is approximately $\frac{1}{3}$ for typical III/V semiconductors. When the thickness of the layer exceeds a certain critical value $d_c \propto \frac{a}{\Delta a}$, then the accumulated elastical distortion energy becomes greater than the dislocation energy and the strain is relaxed by defects. Typical values for the critical layer thickness are $d_c \approx 20$ nm for $\frac{\Delta a}{a} = -1.5$ % and only one monolayer for $\frac{\Delta a}{a} < -6$ % [Gru97].

Under appropriate growth conditions the relaxation of the elastic energy can take place with the development of quite regular 3-dimensional structures. After a critical amount of strained material is deposited, a morphological instability results in the formation of coherent strained islands on the wetted surface. This is called the Stranski-Krastanov growth mode. Formation of 3-dimensional islands leads to a reduction of the strain energy and to an increase of the surface energy as compared to the planar surface case. The first is proportional to the volume of the island, and the latter is proportional to the surface area of the island. If the size of such an island

exceeds a critical value, further growth becomes energetically unfavorable.

This is why the size of the islands does not depend on the amount of material deposited, if the material has enough time to form a field of islands. The amount of the deposited material determines only the surface density of the islands [Gru95].

The size and shape of the island largely depend on the growth conditions (temperature, growth interruption after deposition of the material, V/III equivalent pressure ratio) and on the materials used.

3.2 Sample description

The five samples investigated during this Diplomarbeit were grown by molecular beam epitaxy in Stranski-Krastanov growth mode by Michel Gendry at the Laboratoire d'Electronique-LEAME in the Ecole Centrale de Lyon. The substrate InP is covered by a lattice matched buffer layer of $In_{0.52}Al_{0.48}As$, on which the lattice mismatched InAs is deposited. In contrast to the well studied InAs / GaAs system ($\frac{\Delta a}{a}$ = −6.7 %) the lattice mismatch of InAs / $In_{0.52}Al_{0.48}As$ is only $\frac{\Delta a}{a}$ = −3.0 %. Until now systems with small lattice mismatches have been studied less, because they were considered not to be favorable for the self-organization process. However, in the present study it is shown that nearly a full coverage of the surface with aligned and elongated quantum dots can be achieved.

The growth process was carried out using solid source molecular beam epitaxy. The five samples were grown at 525 °C on a semiinsulating InP (001) substrate [Gen97]. Sample M400 is non-intentionally doped (n.i.d.) and contains one plane of InAs quantum dots. An $In_{0.52}Al_{0.48}As$ buffer layer with 400 nm thickness was grown on the substrate. The $In_{0.52}Al_{0.48}As$ growth rate was 1.01 $\frac{\mu m}{h}$ and the V/III beam equivalent pressure ratio was equal to 23. The buffer layer was followed by 0.9 nm InAs. The InAs thickness of 3 monolayers (ML) is just above the 2D/3D growth mode transition detected by reflected high energy electron diffraction (RHEED) at 2.5 ML. The InAs growth rate was 0.255 $\frac{\mu m}{h}$ and the V/III beam equivalent pressure ratio was equal to 35. The growth was then interrupted and the sample maintained for 120 s at 525 °C under a $5 \cdot 10^{-6}$ Torr arsenic pressure. A 300 nm thick $In_{0.52}Al_{0.48}As$ cap layer was subsequently deposited.

Samples M559, M499, M500 and M586 contain 10 planes of InAs quantum dots separated by 50 nm thick $In_{0.52}Al_{0.48}As$ barriers (see figure 3.1 for a scheme). The growth conditions of these samples were identical, with only the exception of the V/III beam equivalent pressure ratios, represented in table 3.1.

Sample M559 is, like M400, non intentionally doped. Sample M500 is p-doped with Be while samples M499 and M586 are n-doped with Si. In all cases delta doping of the InAlAs barriers is performed 2 nm below each InAs quantum dot layer in order to achieve a sheet carrier density of $5 \cdot 10^{11}$ cm^{-2} for samples M499 and M500 and $2.5 \cdot 10^{11}$ cm^{-2} for sample M586.

Table 3.1: Growth and sample properties.

<table>
<tr><th>Sample</th><th>M400</th><th>M559</th><th>M499</th><th>M500</th><th>M586</th></tr>
<tr><td>number of QD layers</td><td>1</td><td colspan="4">10</td></tr>
<tr><td>Delta doping type</td><td colspan="2">n.i.d</td><td>n</td><td>p</td><td>n</td></tr>
<tr><td>Delta doping density</td><td colspan="2">-</td><td colspan="2">$5 \cdot 10^{11}$ cm^{-2}</td><td>$2.5 \cdot 10^{11}$ cm^{-2}</td></tr>
<tr><td>$(V/III)_{InAs}$</td><td colspan="2">35</td><td colspan="2">90</td><td>60</td></tr>
<tr><td>$(V/III)_{InAlAs}$</td><td colspan="2">23</td><td colspan="2">32</td><td>20</td></tr>
<tr><td>QD surface density</td><td colspan="5">$\sim 7 \cdot 10^{10}$ cm^{-2}</td></tr>
<tr><td>average length of QD</td><td colspan="5">~ 50 nm</td></tr>
<tr><td>average width of QD</td><td colspan="5">~ 25 nm</td></tr>
<tr><td>average height of QD</td><td colspan="5">~ 1.5 nm</td></tr>
</table>

3.3 AFM characterization

First characterizations of the sample were performed with atomic force microscopy (AFM). Figure 3.2 shows an AFM image of a typical uncapped n.i.d. InAs / $In_{0.52}Al_{0.48}As$ structure. The image was taken by M. Gendry at the LEAME. The surface is almost fully covered with InAs quantum dots. They are elongated with the long axis parallel to $[\bar{1}10]$ direction and seem to be lined up also in that direction. Some isolated dots exist as well. Dots of different sizes can be distinguished. The average size is $50 \times 25 \times 1.5$ nm^3. Note that the dots are rather flat. Unfortunately, the exact shapes of the dots cannot be determined from an AFM image.

The island shape and size could be modified after the deposition of the $In_{0.52}Al_{0.48}As$ cap layer. Interdiffusion between the islands and the matrix can occur. Modification of the dots by interdiffusion only involves element III (In, Al) exchanges, since the concentration of As is the same in dots and cap layer. However, the interdiffusion of element III is expected to be negligible at the growth temperature of 525 °C [Bra98]. Studies on other material systems have shown, that significant element III exchanges occur above 650 °C for the InGaAsP / InP system [Fra94, Nak87].

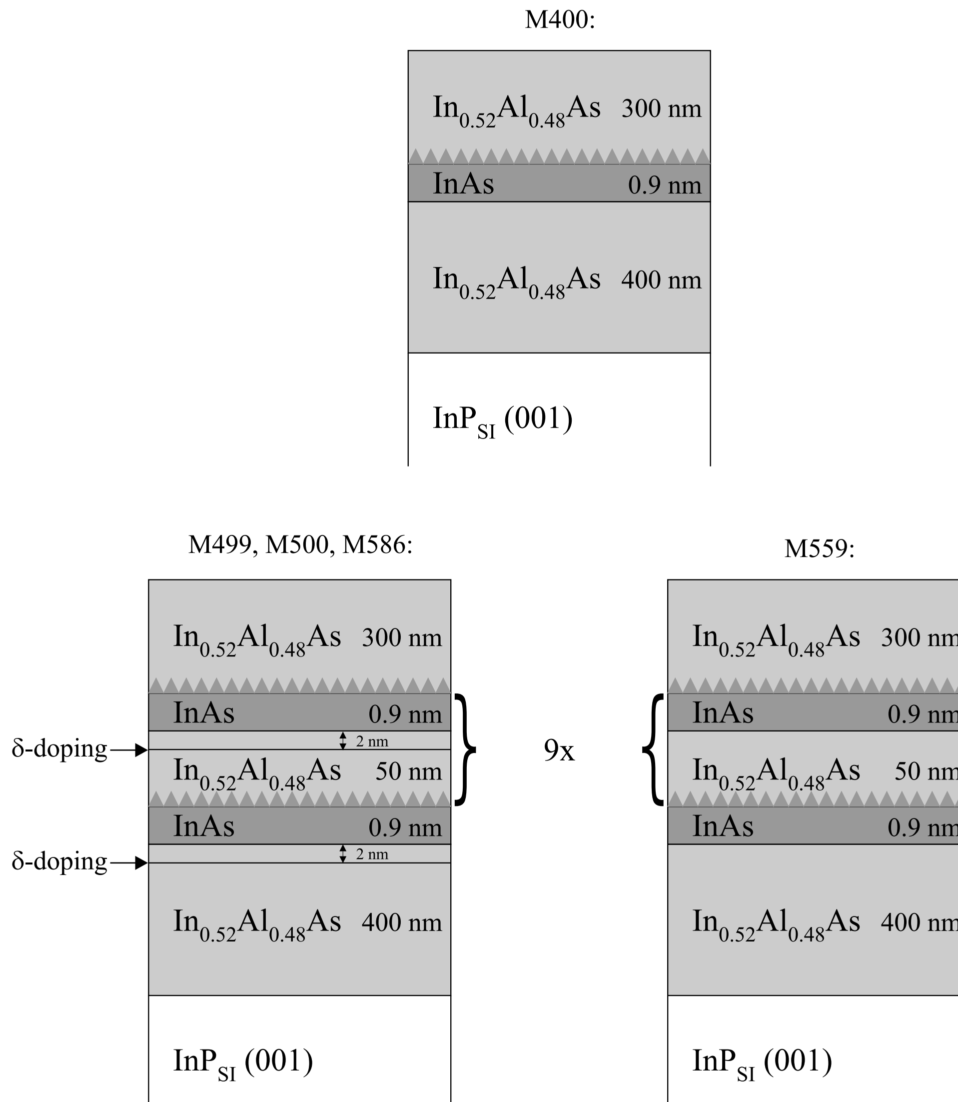

Figure 3.1: Sample layer scheme of the samples M400 (top), M499, M500, M586 (bottom left) and M559 (bottom right).

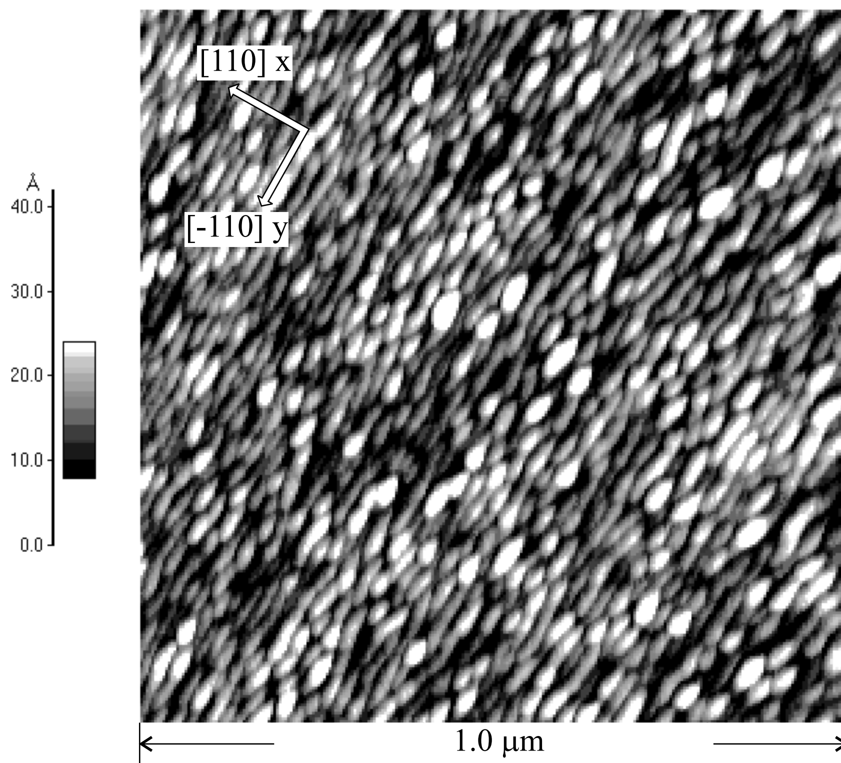

Figure 3.2: AFM image of an uncapped InAs / $In_{0.52}Al_{0.48}As$ *sample.*

Chapter 4

Experimental setup

The quantum dot samples have been characterized by photoluminescence spectroscopy (PL), photoluminescence excitation spectroscopy (PLE) and infrared absorption spectroscopy. The experimental setup and the principal characteristics of these experiments are described in the next sections.

4.1 Photoluminescence

The principle of photoluminescence measurements is to create carriers by optical excitation with a photon energy above the band gap of the quantum structure. Electrons and holes relax to their respective ground states in the conduction and valence band. They can then recombine radiatively as free carriers or excitons. At low temperatures, it is admitted that exciton luminescence largely dominates.

PL spectroscopy allows the following properties to be evaluated:

- The energy position of the PL peaks reflect the strained bandgap plus the confinement energies minus the exciton binding energy.
- The quality of the quantum structure can be evaluated through the width and the intensity of the luminescence signal.
- Optical transitions between excited states may be detected for high excitation intensities.

Figure 4.1 shows the experimental setup for the photoluminescence measurements. The excitation is performed by an Argon-Ion (Ar^{++}) laser, SPECTRA PHYSICS model 2016 at a wavelength of 514 nm. Its output power can be regulated in the range of $\sim$ 5 mW to 6 W.

The beam from the Ar^{++} laser is chopped by a mechanical chopper and then focussed onto the sample using a lens (focal length $f = 10$ cm). The minimum laser spot diameter at the focal point has been determined to be $\sim 50\,\mu$m. The sample is mounted on the cold finger of a liquid nitrogen cryostat. The quartz window of the cryostat is parallel to the sample surface. As there are two different lenses used for the incoming beam and the outgoing radiation, the incoming beam arrives at an angle slightly less than 90 ° while the outgoing light is recovered at normal incidence to the sample surface. The lens collecting the PL light has a focal length of $f = 5$ cm and a focal number $k = \frac{f}{2r} = 2$ (r being the lens radius). The PL beam is then focalized with the focal number of the spectrometer ($k = 4$) onto the input slit of the spectrometer (Jobin Yvon HR 460, with a maximum wavelength of 1.33 μm). A nitrogen cooled Ge detector is used for the detection. Its output signal is detected by a lock-in amplifier at the frequency of the chopper. A computer serves to read the signal from the lock-in amplifier via an IEEE interface. Finally, the spectra are displayed with the Lab-View software package.

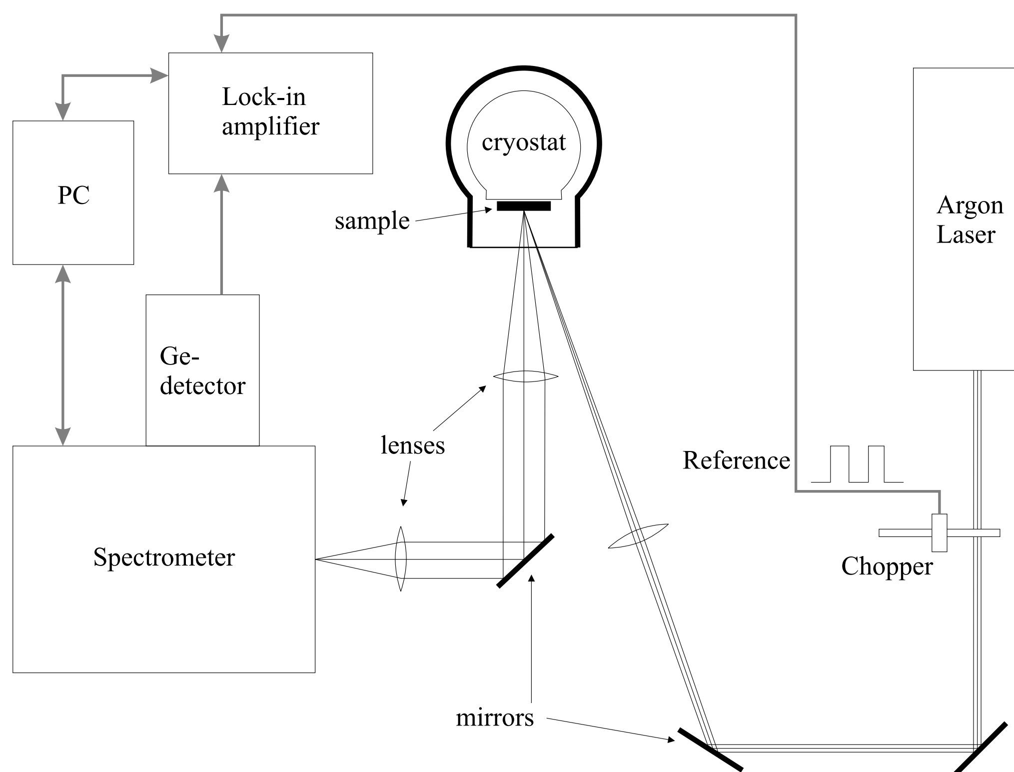

Figure 4.1: Scheme of the PL experiment setup.

4.2 Photoluminescence excitation

The principle of photoluminescence excitation (PLE) spectroscopy measurements is very similar. The detection energy $h\nu_{\text{det}}$ is set at the ground state luminescence. The excitation energy $h\nu_{\text{exc}}$ is varied from $h\nu_{\text{det}}$ to higher energies. If the intraband scattering times are much shorter than the interband recombination times, the ground state luminescence evolves as the joint density of states excited by the excitation source. Under such conditions, the PLE spectrum is analogous to that obtained using absorption spectroscopy. The PLE signal increases each time a new interband maximum is excited. Possible sources are tunable Ti:Sapphire lasers or dye lasers in the 0.4 μm to 1.1 μm range or in longer wavelengths black body sources like halogen lamps, whose light is filtered by a monochromator.

4.3 Intraband absorption

Infrared (IR) spectroscopy is a sound technique to investigate quantum structures, because the wavelength of the IR light corresponds to the energy range of intraband transitions between confined states belonging to either the conduction band or the valence band. A direct measurement of the confinement energies and of the spatial symmetry of the envelope wavefunctions is possible with this technique [Dre94, Sau97].

Different experimental approaches allow intraband absorptions to be measured. They can, for example, be studied with laser spectroscopy (continuous CO_2 [Jul91]) or with a Fourier transform infrared spectrometer (FTIR). The latter is appropriate when studying a larger frequency range. The experiments described here have been carried out with a FTIR, a Biorad FTS-60A.

4.3.1 FTIR spectrometer

Principle

A Fourier spectrometer's main components are a Michelson interferometer, an IR source, an IR detector, electronics and an informatic system.

The Michelson interferometer consists of a fixed mirror, a moving mirror and a beamsplitter (Figure 4.3). After being reflected or transmitted off the beamsplitter, the two beams recombine there again after reflection on the mirrors. The recombined beam passes through the sample chamber and is detected on an IR detector.

If the moving mirror is at the same optical distance from the beamsplitter as the fixed mirror, a

maximum positive interference takes place in the recombined beam, because the path difference is zero for all wavelengths. But if the moving mirror is displaced by a distance D, the two beams cover different distances and the intensity of the interfered beam changes. The phase difference depends on the displacement of the mirror D as

$$\phi = \frac{2\pi D}{\lambda} = 2\pi\sigma D, \tag{4.1}$$

where $\sigma = \frac{1}{\lambda}$ is the wavenumber.

Assuming the transmission coefficent of the beamsplitter to be 50 %, the detected intensity on the detector for a wavenumber σ is [Wu96]:

$$I = 0.5 I_0 (1 + \cos 2\pi\sigma D). \tag{4.2}$$

The detector signal hence represents the interference signal of the two beams coming from the fixed and moving mirror and is therefore dependent on the position of the moving mirror. The interferogram of a monochromatic wave with wavelength λ is a sine function with period $\frac{\lambda}{2}$. If the input beam is not monochromatic, but a spectrum with a spectral density $S(\sigma)$ (which is, for a FTIR spectrometer, in the IR region), the detected intensity is:

$$I(D) = 0.5 \int S(\sigma)[1 + \cos(2\pi\sigma D)]\, \mathrm{d}\sigma. \tag{4.3}$$

After eliminating the constant part of the signal, which is independant of D, the source spectrum can be obtained by an inverse Fourier transformation:

$$S(\sigma) = 2 \int I(D) \cos(2\pi\sigma D)\, \mathrm{d}D. \tag{4.4}$$

The transmission of a sample can be measured by dividing the spectrum $S(\sigma)$ of the sample by a *background* spectrum $S_0(\sigma)$, which corresponds to a reference spectrum of the source without the sample, but which takes into account the reflectivity of the mirrors and the beamsplitter as well as the atmospheric absorption.

Configuration

The moving mirror, which is displaced by a linear motor, modulates the IR source (glow bar). The result is an interferogram, which is transformed into a spectrum by a computer after an analog signal treatment and the inverse Fourier transformation. The movement of the mirror is monitored by an internal HeNe laser, whose beam passes also through the spectrometer. A

photodiode detects the intensity oscillations during the mirror movement and allows the position of the mirror to be precisely controlled. The spectral range of the spectrum depends on the distance ΔD between two sampling positions, where the intensity is measured. Usually an under sampling ratio UDR = 2 was chosen. This means, that a measurement is taken every two periods of the HeNe oscillations. The resulting spectral range is from 0 to $(2 \cdot 632.8\ \mathrm{nm})^{-1} \approx 7900\ \mathrm{cm}^{-1}$.

There are two function modes of the FTIR spectrometer: rapid scan and step scan. In the rapid scan mode, the mirror rapidly oscillates between the limits. The sampling of all points is done during one pass of the mirror. This means that the measuring time at each point is quite short and there is much noise in the spectrum. To obtain a better signal to noise ratio, a mean value of multiple spectra is taken. The rapid scan mode is used for standard spectroscopy because of the following reasons: reduction of the dynamical range of the interferogram with electrical filters before the analog-digital conversion, the elimination of low frequency noise (source fluctuations, electronic and detector deviations, mechanical vibrations etc.) and faster measurements. In the step scan mode, the mirror is displaced from one sampling position to the next, after being held stationary for the measuring time for each point. The measuring time depends on the signal to noise ratio and is usually in the range of 0.1 s/step to 10 s/step. In addition, it is possible to modulate the signal (either the source or the transmission of the sample by optical excitation) in the step scan mode with a high frequency, without any interference with the moving mirror. This permits the use of a lock-in amplifier for experiments with low signals.

In general, the transmission spectra were achieved in rapid scan mode, while the photo-induced absorption spectra were performed in step scan mode.

For the signal detection, a broadband MCT (mercury cadmium telluride) detector with a cut-off wavenumber of $500\ \mathrm{cm}^{-1}$ was used.

4.3.2 Photo-induced experiments

The absorption of undoped samples can be measured if carriers are generated in the conduction and valence bands through interband excitation. This is performed either with an Ar^{++} laser or with a Ti:Sapphire laser for non-resonant pumping below the bandgap of the substrate to pump just the confined structure.

To increase the absorption and the observed signals, the facets of the sample are optically polished at a 45° angle in order to permit several passages of the IR beam through the active layers of the sample (see figure 4.2). It is necessary to polish the back side of the sample (substrate) in IR optical quality. Instead of just one passage of the IR beam through the quantum structures in

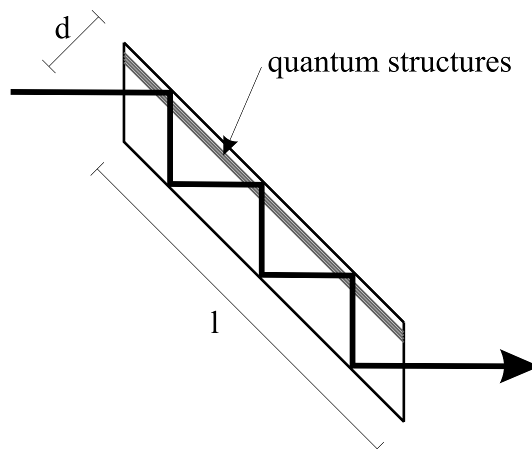

Figure 4.2: Sample in a 45 ° *waveguide configuration.*

the normal-incidence configuration,

$$n = \frac{\ell}{d} \tag{4.5}$$

passes can be achieved in the 45 ° setup (with ℓ and d being the length and the thickness of the sample, respectively, and with ℓ being an even integer multiple of d.).

Figure 4.3 shows the experimental setup for the photoinduced experiments with the FTIR. The pump laser is mechanically chopped and focussed onto on the surface of the sample. A mercury cadmium telluride (MCT) detector is used for the detection of the infrared beam. The signal is amplified by a lock-in amplifier and finally the Fourier transformation is performed.

Because it is a differential technique, photo-induced absorption spectroscopy allows the measurement of extremely faint absorptions. In the actual experimental setup, absorptions lower than 10^{-5} can be easily measured.

4.3.3 Background spectra

The choice of the background spectrum needs special attention. If, for example, only the absorption of a quantum structure in a sample is to be measured, one must eliminate the substrate absorption and Fabry-Perot fringes. The best solution is to have a background spectrum with a sample with the same optical thickness but without the quantum structure or with all carriers depleted.

For strongly polarized absorption, it is also possible to record the background spectrum using the perpendicular polarizations (see section 6.2).

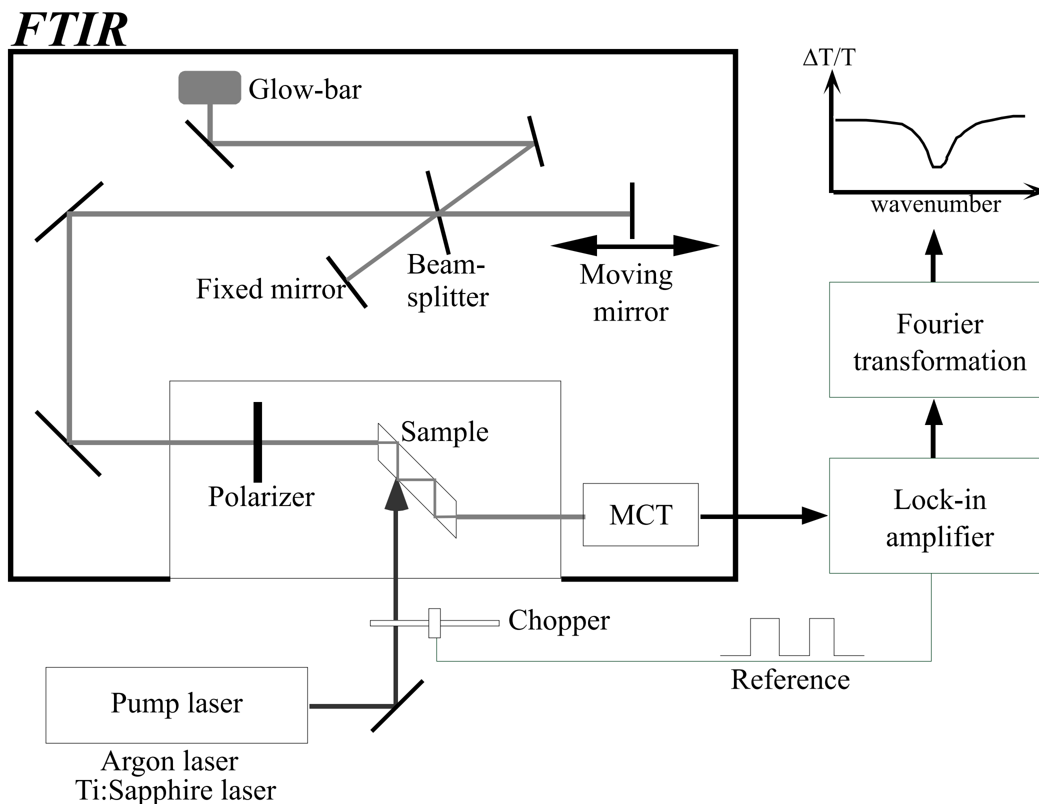

Figure 4.3: Experimental setup for infrared experiments.

Because it is a differential technique, photo-induced absorption spectroscopy (section 4.3.2) eliminates the difficulty of measuring a background spectrum on a different sample. Indeed the background absorption of the substrate as well as the Fabry-Perot interferences can be easily measured by simply suppressing the excitation source.

Chapter 5

Photoluminescence results

The photoluminescence (PL) and photoluminescence excitation (PLE) spectroscopic results are presented in this chapter. The PL experiments serve to obtain information on the confinement type of the InAs / $In_{0.52}Al_{0.48}As$ samples. The size distribution of the quantum structures can also be tested with this experimental technique. By changing the excitation intensity, information about excited states and band filling effects can be obtained. In addition, PLE experiments can be used to identify the excited states of the structure.

5.1 Photoluminescence

Figure 5.1 shows the PL spectrum of the non-intentionally doped (n.i.d.) sample M400 at a temperature of 4 K. The excitation was performed by a continuous Ar^{++} laser with an intensity of 15 $\frac{W}{cm^2}$. This spectrum was, as well as the PLE spectra shown in figure 5.4, obtained by T. Benyattou (Laboratoire de Physique de la Matière-LPM, INSA de Lyon).

A structured PL band is detected between 0.95 eV and 1.3 eV. The full width at half maximum (FWHM) of the band is about 170 meV. We have fitted the spectrum with five Gaussian peaks labelled a) to e) (table 5.1 and dotted lines in figure 5.1). The FWHM of these peaks is around 50 meV, except for peak e), where it is 70 meV.

There are two possibilities to interpret the observed PL structure. First, the five peaks can result from transitions from the ground electron to the ground valence band state for 5 different sizes of quantum dots. Larger dots have lower energy levels (equation 2.21) and would therefore contribute to the low-energy side of the spectrum, whereas smaller dots contribute to the peaks on the high-energy side of the spectrum. A second possibility is, that the higher-energy peaks result from transitions between excited states. This would require complete filling of the electron

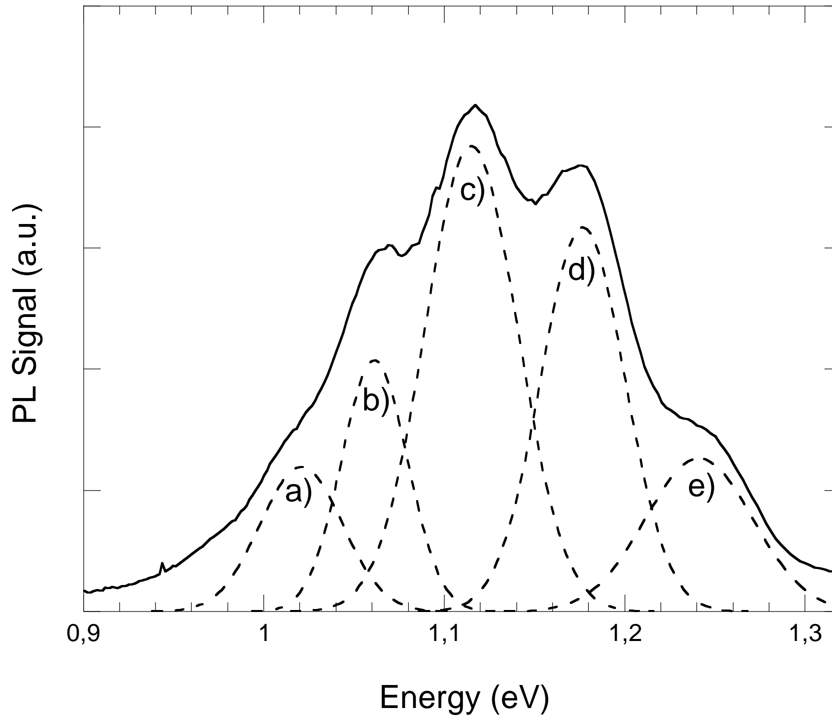

Figure 5.1: Photoluminescence of the n.i.d. sample M400 at $T = 4.2$ K. The dotted peaks a) to e) represent the fitted Gaussians (table 5.1).

and hole ground states and partial filling of the excited states [Lip95] (which is unlikely at the low excitation intensity used in the experiments [Sau97]) and/or very slow intraband relaxation times with respect to the interband recombination times ($1-10\,\mu$s) [Muk96].

Phonon bottleneck effects are expected to occur in low dimensional structures [Ben91]. This translates into long intraband scattering times and long dephasing times. As a consequence, a single quantum dot is expected to have a very narrow PL emission of the order of 0.1 meV [Bas94]. The observed peaks are a superposition of a high number of very sharp PL lines, coming from individual dots. The PL spectrum reflects the size fluctuations (Gaussian distributions with FWHM of $\sim$ 50 meV) around each of the five average sizes of dots in the sample.

An explanation for the 5 different average sizes of the quantum dots could be monolayer fluctuations of the wetting layer during the growth process.

Table 5.1: Positions of the gaussian peaks fitted in the PL spectrum of figure 5.1.

peak	position (meV)	FWHM (meV)	rel. intensity
a)	1021	54	0.31
b)	1061	43	0.54
c)	1115	61	1.00
d)	1177	55	0.83
e)	1241	70	0.33

5.1.1 Uniformity of the sample

We have studied the size distribution of the quantum dots and the uniformity of the sample by carrying out PL spectra at different locations on the sample M400. The excitation intensity of the Ar^{++} laser was $\sim 500\ \frac{W}{cm^2}$ and the sample was at a temperature of $T = 77$ K. Figure 5.2 shows 7 different PL spectra taken at 7 distinct points (A-G) on the surface of the sample (with a size of 8×10 mm). The points are separated about 2 mm from each other. It can be seen that the spectra are similar, but the relative intensities of the peaks change whereas their energy positions do not. Since the experimental conditions are the same for all of the spectra, the differences between the spectra can only be explained by structural differences of the excited quantum dots.

All the spectra show that the PL size distribution of the quantum dots consists of several Gaussian like peaks, which are centered on *preferred* dot sizes.

5.1.2 Influence of excitation power

The dependence on excitation intensities have also been measured.

Figure 5.3 shows four PL spectra of the sample M400. They were recorded at a temperature of 77 K in the configuration shown in figure 4.1. The optical excitation was carried out by an Ar^{++} laser at a wavelength of 514 nm. The different laser intensities are indicated for each spectrum.

It can clearly be seen that for low excitation intensities the relative intensities of the low-energy peaks in the spectrum are larger, while the relative intensities of the high-energy peaks increase with pump power.

When looking at the spectrum with the lowest excitation energy in figure 5.3, peaks a), b) and

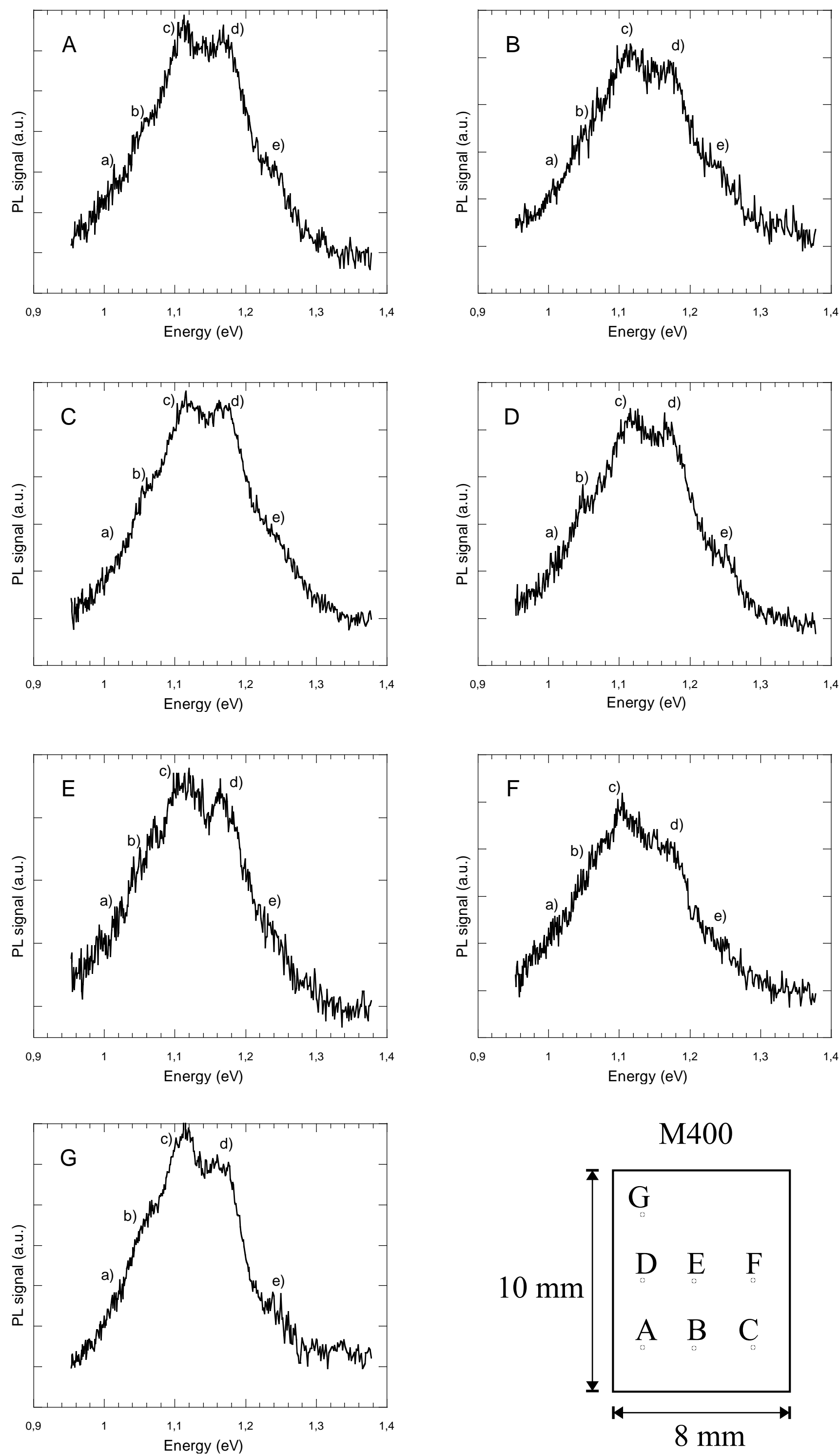

Figure 5.2: Photoluminescence of the n.i.d. sample M400 at 77 K. *7 different spectra were done at different spots of the sample (scheme: bottom right). The excitation intensity was* $\sim 500\ \frac{\mathrm{W}}{\mathrm{cm}^2}$.

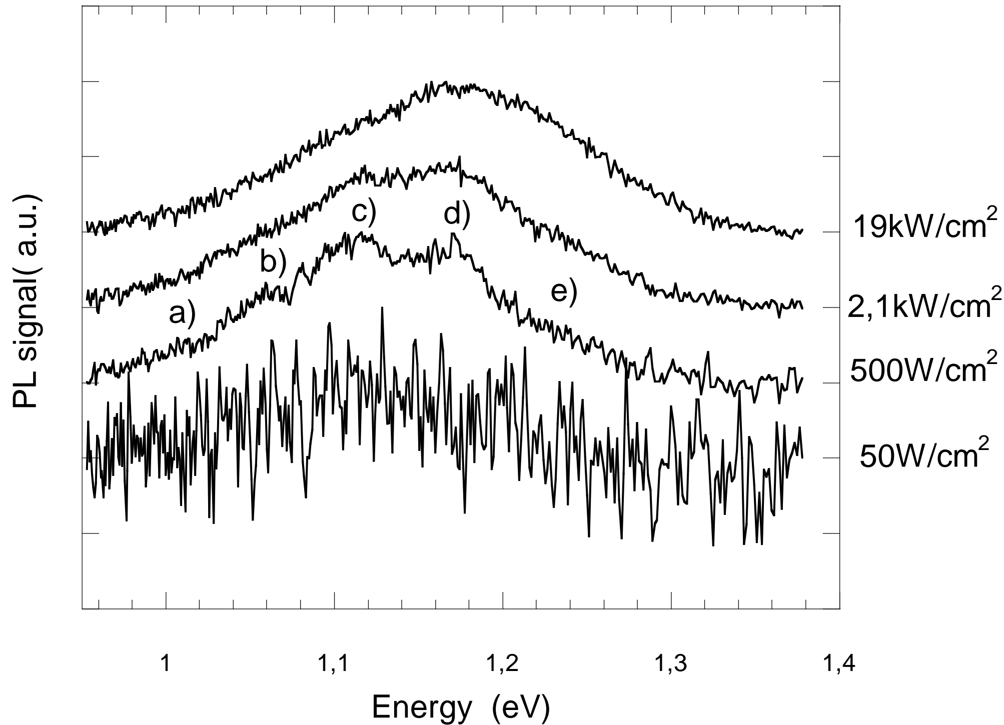

Figure 5.3: Photoluminescence of the n.i.d. sample M400 at $T = 77$ K. *The* Ar^{++} *laser excitation intensity is marked next to each spectrum. The spectra are normalized and horizontally shifted for better visibility.*

c) have the highest relative intensities. They correspond to ground state transitions of quantum dots with large sizes (and low energy levels). When increasing the pump power, the contribution of peaks d) and e) to the PL spectrum increases. They can have their origin either in ground state transitions of smaller dots or in excited transitions.

This can be interpreted in the following way: The excitation by the Ar^{++} laser creates carriers, which relax radiatively and non-radiatively, until they are captured by a quantum dot, where they relax to the ground (electron or hole) state. The larger dots have lower energy states and are populated first. The intraband relaxation times are normally much shorter than the interband transition times. This means, the carriers stay for a certain time in the ground state, before they recombine under the emission of the observed PL. If the excitation intensity is high enough to create more carriers per unit time than the recombination rate, the ground state fills up with carriers.

Since in a quantum dot an energy level is filled with only two carriers (spin up and down, respectively), when pumping strongly enough, the ground state of the large dots can be filled and smaller dots or the higher states are then populated.

An other phenomenum may take place in quantum dots: the phonon bottleneck [Muk96, Boc90, Ben91]. It is predicted by this theory that the discrete levels in quantum dots hinder carrier relaxation towards the ground state, because it is unlikely that phonon relaxation processes have just the exact energy difference between the discrete energy levels. Thus phonon relaxation can not take place. However, there are still debates about the possibility of rapid carrier relaxation mediated by Auger processes [Boc92], multiphonon processes [Ino92] or electron-hole interaction [Boc93]. Nevertheless, the phonon bottleneck effect would emphasize the observation of excited transitions in the PL spectra, since the relative number of electrons in the excited states would be increased.

5.2 Photoluminescence excitation

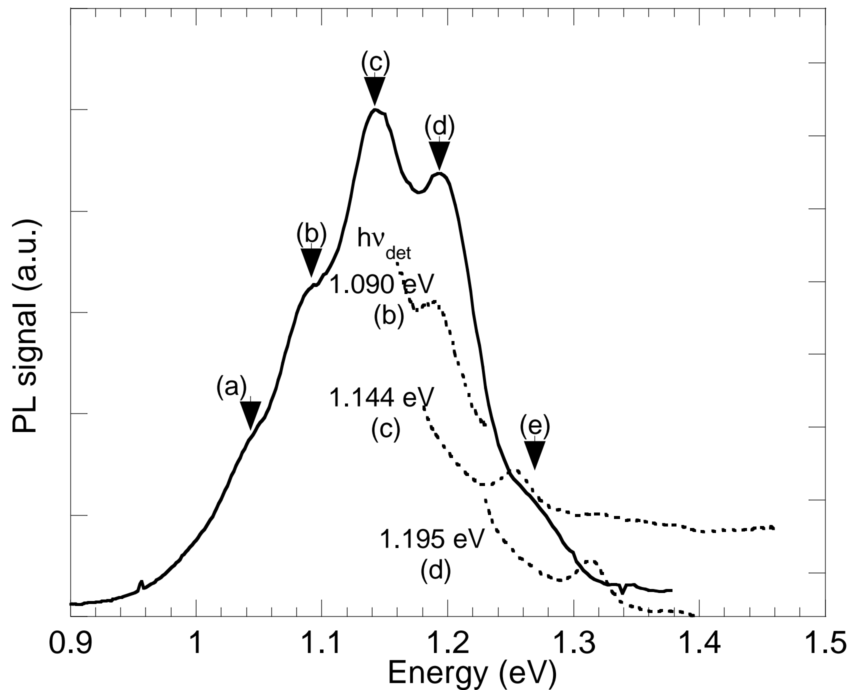

Figure 5.4: Photoluminescence of the n.i.d. sample M559 at $T = 4.2\,\mathrm{K}$ *under* $15\ \frac{\mathrm{W}}{\mathrm{cm}^2}$ *excitation by an* Ar^{++} *laser (full curve). The dotted curves are PLE spectra with the detection photon energy set at peaks b), c) and d), respectively. The PLE spectra are horizontally shifted for better visibility.*

Figure 5.4 shows the PL spectrum of the n.i.d. sample M559, which has the same composition as M400, except that it possesses 10 layers of quantum dots (instead of only one for M400)

to achieve higher PL intensities. In the same figure, three PLE spectra with detection photon energy set at peaks b), c) and d), respectively, are shown. The sample was at a temperature of 4.2 K and the excitation intensity for the PL was 15 $\frac{\mathrm{W}}{\mathrm{cm}^2}$.

The PL spectrum has the same characteristics as the spectrum of the sample M400 (figure 5.1). However, the energy positions of the five fitted Gaussian peaks are slightly different, which is probably due to growth condition differences between the two samples.

The PLE spectra of peaks b), c) and d) clearly show only one excited state absorption peak, which is shifted to higher energies from the ground state luminescence by 101 meV, 109 meV and 120 meV, respectively. These values reflect both the electron and the heavy-hole quantum confinement. The smaller dots have larger energy shifts in agreement with equation (2.21).

PLE spectra of peaks a) and e) were also performed, but they did not clearly reveal any excited states PL.

It is clear from the PLE results that peaks b), c) and d) arise from the ground state transition of quantum dots with different sizes. It is also clear that excited states of dots c) and d) contribute to peak e). This observation is in agreement with the PL evolution with excitation intensity.

5.3 Conclusion

The PL experiments show that

- quantum dots on the sample have different volumes.
- the quantum dot sizes have a distribution, which is composed of five Gaussians.
- when exciting with high intensities, the filling of the larger dots and transitions between excited states can be observed at high energies.

The PLE experiments show that there is only one excited state for each dot size and confirm that there are preferred sizes of the quantum dots. However the high energy peak contains significant contributions from excited states.

At this point, it would be interesting to compare calculations of the energy levels of the dots with experimental data. Calculations for the new InAs / $In_{0.52}Al_{0.48}As$ system have not yet been performed. Moreover, energy calculations are only valid if the exact shape of the dots is known, which is not the case at the early stage of the research for this material system.

Chapter 6

Intraband spectroscopy

In this chapter the results of infrared (IR) spectroscopy are presented and discussed. The first section of this chapter describes the experiments with the undoped sample to show the existence of an intraband transition in the InAs / $In_{0.52}Al_{0.48}As$ system. In the second section further experiments with doped samples are presented to obtain information, for example, about the carrier type involved in the resonance and absolute absorption values. The last section deals with intraband emission experiments of an undoped sample.

The experiments were performed with a Fourier Transformation Infrared (FTIR) spectrometer, as discussed in section 4.3.

6.1 Photo-induced intraband absorption of the n.i.d. sample

The IR spectroscopy experiments described in this section were performed on the n.i.d. sample M400. The photo-induced absorption technique is used to create carriers in the undoped sample by excitation with an Ar^{++} laser.

6.1.1 Zigzag configuration

Because of the expected low absorption signals in the sample with only one layer of quantum dots, the sample was polished in a 45° zigzag configuration to multiply the passes of the IR beam through the quantum structures. The absorption is measured for the two polarizations s and p, which are perpendicular and parallel to the plane, respectively, in which the IR beam traverses the sample in zigzag. The decomposition of the polarizations s and p in sample coordinates x, y and z, which depends on which facets of the sample are polished at 45 °, is for the first set of

experiments (figure 6.1):

$$\begin{aligned} s &= s_x &= x, \\ p &= p_{yz} &= \tfrac{1}{2}(y+z). \end{aligned} \tag{6.1}$$

This means, that the p polarization of the IR beam contains components of both the polarizations y, which is parallel to the elongation direction of the dots, and z, which is parallel to the growth axis of the sample. The length of the sample is $l = 3$ mm and its thickness is $d = 0.3$ mm. This means that the IR beam passes the quantum dot layer about 10 times during its passage through the sample (equation (4.5)).

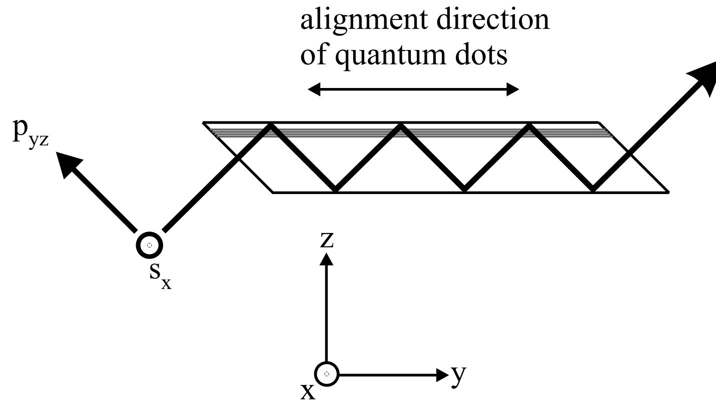

Figure 6.1: Decomposition of the polarizations s_x and p_{yz} of the IR beam into the sample directions x, y and z: $s_x = x$ and $p_{yz} = \frac{1}{2}(y+z)$.

Figure 6.2 shows three photo-induced FTIR absorption spectra of the undoped sample M400 in zigzag configuration at $T = 77$ K for three different excitation intensities. In each graph the two spectra for the polarizations s_x and p_{yz} are represented. In all three spectra an IR absorption peak can be distinguished at an energy of 91 meV for the s_x polarization. The FWHM of the peak is about 15 meV. In the y and z polarization no resonances can be found. At high excitation intensities the width of the peak increases towards the high energy side, which could be caused by the population of smaller QDs with higher energy states.

At low energies (< 85 meV) all graphs show an increase of the absorption in both polarizations. These peaks do not have their origin in infrared transitions inside the sample, but they are artifically created when the spectra are divided by their backgrounds. This can be explained as follows when looking at a background spectrum.

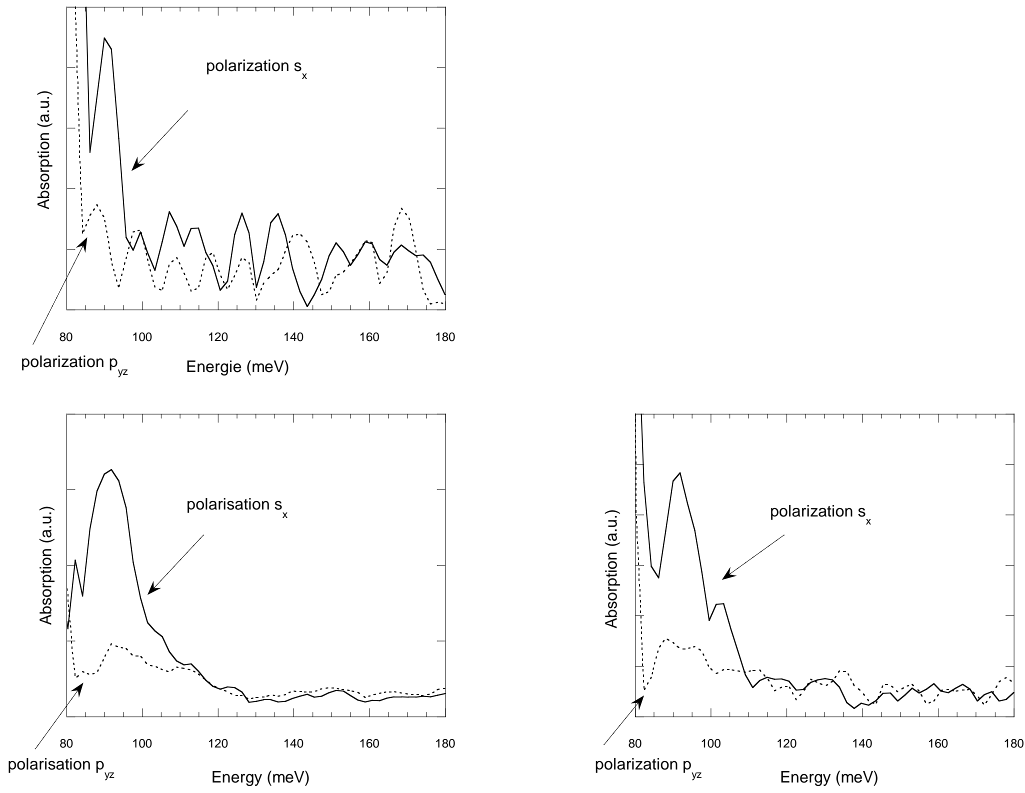

Figure 6.2: Photo-induced intraband absorption the sample M400 (zigzag) at $T = 77\,\mathrm{K}$ *under a respective excitation of* $15\,\frac{\mathrm{W}}{\mathrm{cm}^2}$ *(top left),* $50\,\frac{\mathrm{W}}{\mathrm{cm}^2}$ *(bottom left) and* $70\,\frac{\mathrm{W}}{\mathrm{cm}^2}$ *(bottom right).*

6.1.2 Background

As mentioned in section 4.3.3, an absorption spectrum of the quantum dots can only be obtained by comparing an absorption measurement of the QDs with a background measurement of the transmission of the source, the spectrometer, the atmosphere and the sample substrate. The QD absorption spectrum without the other influences is obtained by dividing the spectrum of the QDs through the background transmission spectrum.

In the case of photo-induced experiments, it is possible to obtain only the substrate transmission spectrum, without absorption of the QDs, by simply not exciting any carriers in the undoped sample so that no absorption can take place. Figure 6.3 shows such a background transmission spectrum of the sample without optical excitation. Three very strong absorption peaks appear at energies of 78 meV, 82 meV and 86 meV. They can be attributed to the absorption of combinations of two transverse optical (TO) phonons, one longitudinal optical (LO) plus one TO phonon and two LO phonons, respectively, in the InP substrate (appendix A). Because these

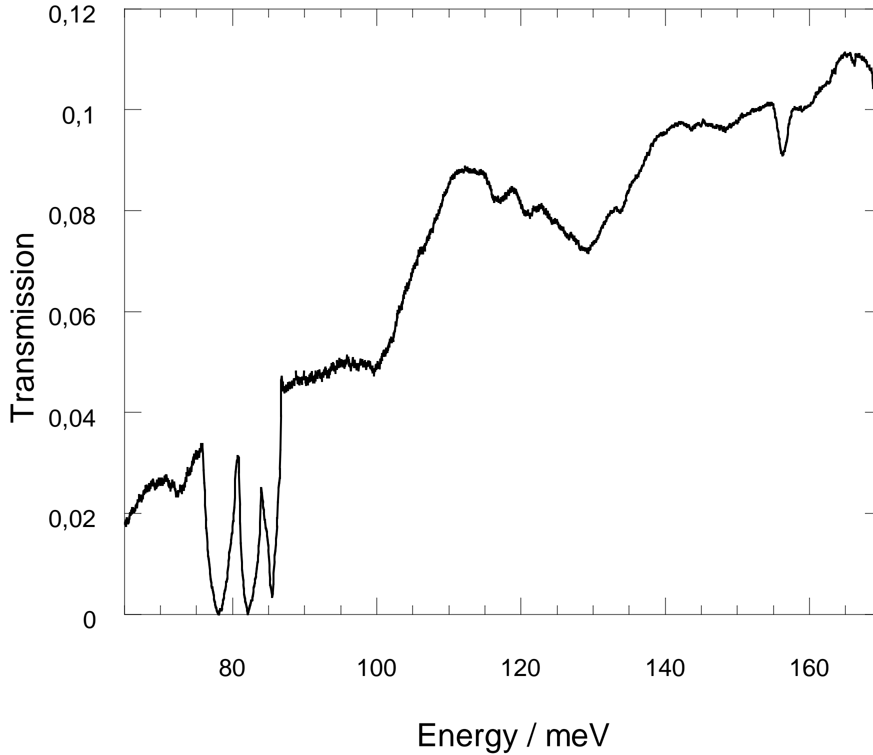

Figure 6.3: Infrared transmission of the sample M400 at $T = 77$ K *in zigzag configuration (background spectrum).*

peaks absorb nearly all of the IR beam, the transmission intensity is nearly zero at the energies of these phonon combinations. When the quantum dot absorption spectrum is divided through the background spectrum, a division nearly by zero takes place at the InP phonon peak energies. This is why at low energies artificial peaks appear in the IR absorption spectrum of the quantum dots.

6.1.3 Confirmation of the absorption in different configurations

To confirm the existence of a x polarized intraband resonance, separate experiments were carried out with the sample's other two opposite facets polished at 45 ° (figure 6.4). In this configuration no absorption is expected in $s = s_y = y$ polarization, but a peak is expected in the $p = p_{xz} = \frac{1}{2}(x + z)$ polarization. Figure 6.5 shows the photo-induced absorption spectrum of the sample M400 in this configuration at $T = 300$ K. In p_{xz} polarization the resonance can be distinguished at 90 meV. The signal to noise ratio of the peak is not as good as in figure 6.2 for the same experimental conditions, which can be explained by two reasons: (a) the absorption from the ground state is less efficient at $T = 300$ K than at $T = 77$ K because there are fewer

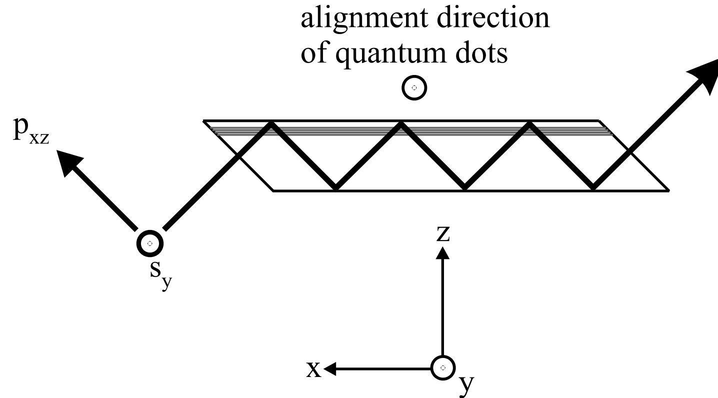

Figure 6.4: Decomposition of the polarizations s_y and p_{xz} of the IR beam into the sample directions x, y and z: $s_y = y$ and $p_{xz} = \frac{1}{2}(x + z)$.

carriers in the ground state and (b) the p_{xz} polarization contains only half of the component of x polarization.

The existence of the x polarized absorption can thus be confirmed. Separate photo-induced measurements on the InP substrate do not show any resonances. This means that the observed resonance is due to an intraband transition of the InAs / $In_{0.52}Al_{0.48}As$ quantum dots.

6.1.4 Normal incidence

The intraband absorption of the sample M400 is strong enough to be detected in normal-incidence configuration. In this case, the IR beam propagates in the sample along the growth direction z. Therefore only one passage through the quantum dot layer is effectuated, which decreases the absorption of the quantum structures by a factor of 10 compared to the 45° zigzag configuration. The two polarizations x and y of the IR beam directly correspond to the sample coordinates. Figure 6.6 shows two photo-induced absorption spectra of the sample M400 in a normal-incidence configuration. One of the spectra was recorded at $T = 77$ K, the other at $T = 300$ K. Each spectrum shows the x polarization (solid line) and y polarization (dotted line).

In both spectra the x polarized resonance can be found, while in y polarization no absorption can be distinguished. The energy position of the peak does not change with the temperature, as well as the full width at half maximum (FWHM), which is in both cases ~ 20 meV. The constant width of the peak at both temperatures suggests that the homogeneous linewidth is very small and that the inhomogeneous broadening due to size fluctuations dominates.

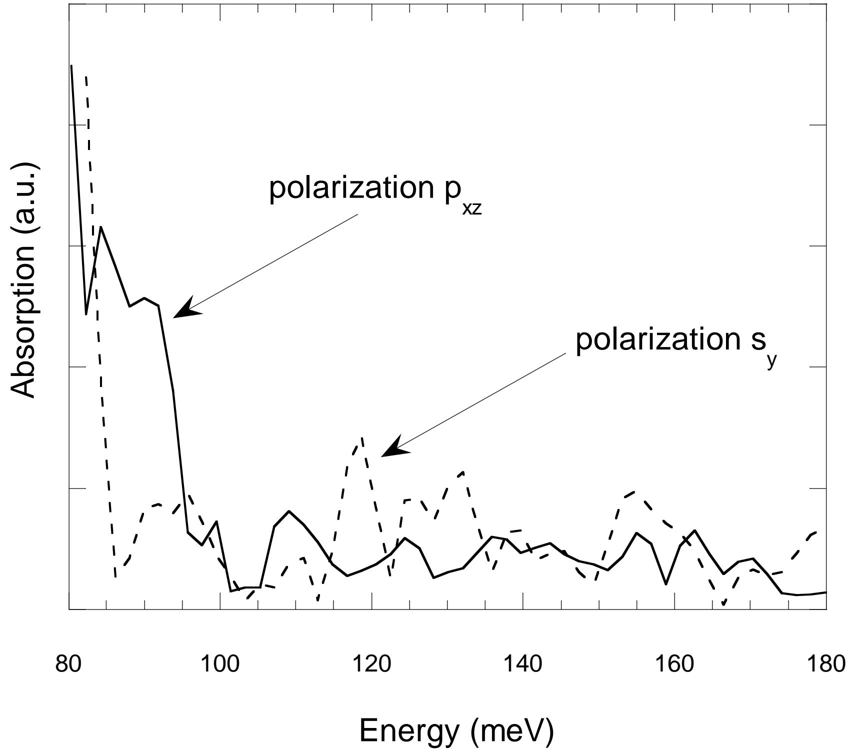

Figure 6.5: Infrared transmission of the sample M400 at $T = 300$ K *in* s_y *zigzag configuration at an excitation intensity of* $20\ \frac{\text{W}}{\text{cm}^2}$.

6.1.5 Conclusion

All the photoinduced spectra of the sample show an IR absorption at $\sim$ 90 meV, which is polarized in the x direction. No resonances polarized along the y axis or the z axis are observed within the investigated 60 meV to 500 meV range within the sensitivity of the measurements. The low excitation energy spectra populate only the ground energy level. The fact that the absorption is polarized indicates that an intraband absorption from the ground state to an excited state confined along the [110] direction has been observed. However it is not clear at this stage, whether or not the transition occurs in the conduction band or valence band.

The polarization of the absorption leads to the conclusion that the dipole of the intraband transition is parallel to the x axis in the quantum structure layer, which is a signature that the excited state is confined in the layer plane.

The size distribution of the quantum dots revealed by the PL experiments cannot be resolved in the FTIR spectra within the energy resolution of the spectra (4 meV). However, the FWHM of $\sim 15 - 20$ meV of the resonance corresponds to the shift of energy difference between the ground state and first excited state for different dot sizes in the PLE experiments, which is from

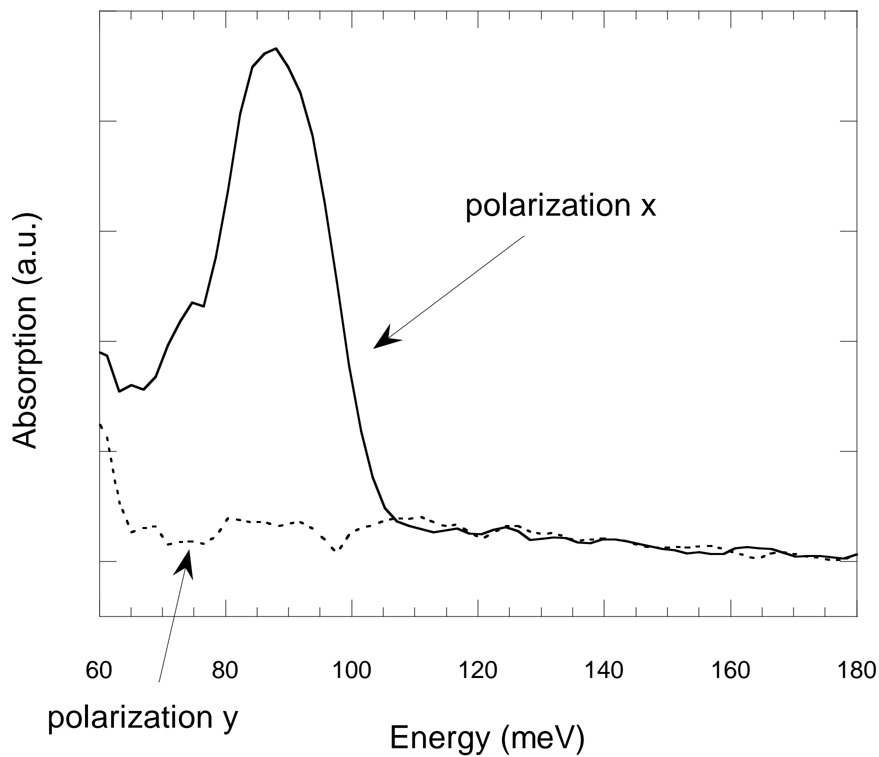

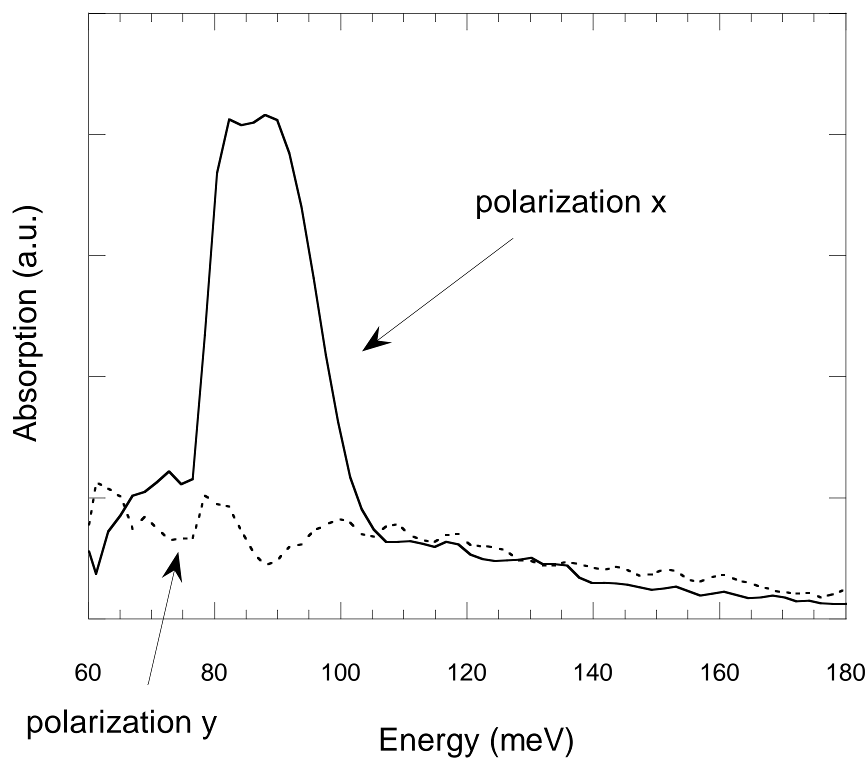

Figure 6.6: Photo-induced intraband absorption of the sample M400 in normal incidence configuration at $T = 77\,\mathrm{K}$ *(top) and* $T = 300\,\mathrm{K}$ *(bottom). The excitation intensity was* $10\,\frac{\mathrm{W}}{\mathrm{cm}^2}$.

101 meV to 120 meV.

6.2 Intraband absorption of the doped samples

The photoinduced spectra do not show whether or not the intraband absorption occurs in the valence band or in the conduction band. FTIR absorption measurements of the p-doped and n-doped samples were performed in order to assess the origin of the resonance.

FTIR spectra of the p-doped sample M500 in normal incidence configuration at $T = 300$ K did not show any resonance in the 60 meV to 500 meV range. However, spectra of the n-doped sample M499 show an x polarized infrared resonance (figure 6.7). The fact that the transition from the ground state to the excited state, oberved on the undoped sample, is also detected in the n-doped but not in the p-doped sample, indicates that the absorption originates from an intraband transition in the conduction band of the InAs dots.

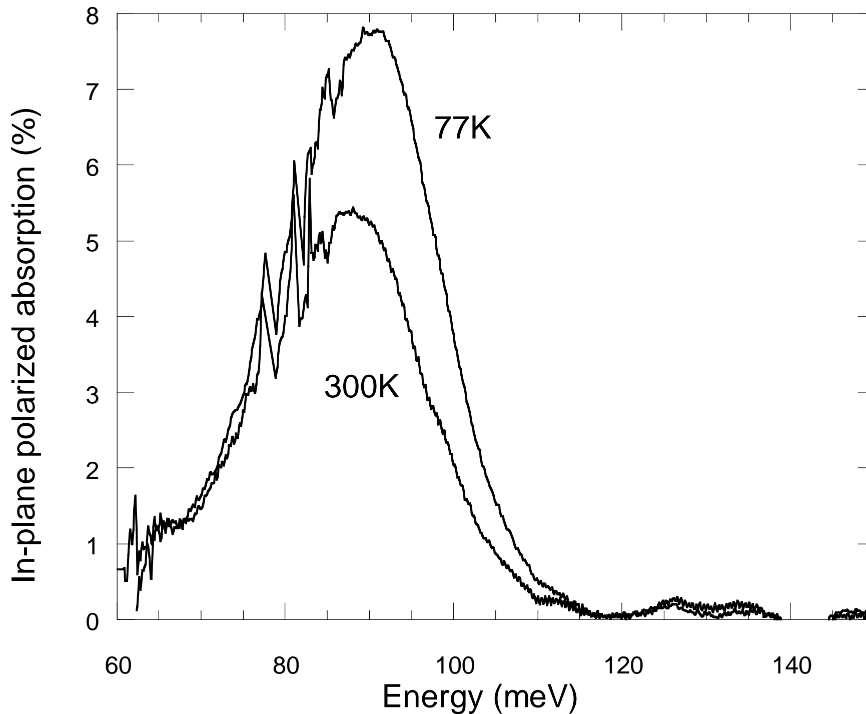

Figure 6.7: Intraband absorption at normal-incidence of the n-doped sample M499 at $T = 77$ K and $T = 300$ K.

Figure 6.7 presents the absorption spectra of sample M499 (n-doped) in x polarization divided by the spectrum in y polarization, which serves as background spectrum (because no QD ab-

sorption takes place in this polarization, as shown by the photo-induced experiments). The spectrum at $T = 77$ K shows an absorption peak at 91 meV. The absorption at maximum is of the order of $\frac{\Delta t}{t} = 7.7$ % (with t being the transmission of the sample). It should be emphasized that this rather large value is achieved at normal incidence with a sample containing only 10 layers of dots. The absorpion peak at room temperature is located at 88 meV and has a maximum absorption of $\frac{\Delta t}{t} = 5.3$ %. The integrated intensity of the peak drops by 32 % from 77 K to 300 K. The FWHM is 22 ± 0.5 meV at both temperatures. This confirms within our resolution that the linewidth of the absorption is temperature independent and therefore dominated by inhomogeneous broadening due to a size distribution. The intraband resonance experiences a slight red-shift of 3 meV when the temperature is increased from 77 K to 300 K, which is typical of intraband transitions [All88].

Assuming all impurities in the delta-doping layer are ionized and accounting for the measured absorption and linewidth, the equivalent absorption cross-section σ at normal incidence for one plane of InAs dots is deduced to be

$$\sigma = \frac{\alpha}{n} \approx \frac{\frac{\Delta t}{t}}{n_{2D} N} \approx 1.5 \cdot 10^{-14}\ \mathrm{cm}^2, \tag{6.2}$$

where $\alpha \approx \frac{\Delta t}{tL}$ is the absorption coefficient, $n = \frac{n_{2D}}{L}$ the carrier density in the absorbing volume, n_{2D} the surface density of carriers (delta doping density), N the number of quantum dot layers and L the thickness of the absorbing volume (which disappears in equation (6.2)).

The average dipole length $\langle x \rangle$ associated with the intraband transition is estimated to be

$$\langle x \rangle = \frac{\mu}{e} \approx 21.3\ \text{Å}, \tag{6.3}$$

where

$$\mu = \sqrt{I \frac{\varepsilon_0 c \hbar \tilde{n}}{\pi E n_{2D} N}} \tag{6.4}$$

is the intraband dipole moment. I is the integrated absorption intensity, ε_0 the dielectric constant, $\hbar$ the Planck constant, $\tilde{n}$ the refractive index of the quantum dots and E the energy difference of the transition.

The oscillator strength f is then estimated to be

$$f = \frac{2 m_0 E}{\hbar^2} \langle x \rangle \approx 10.7, \tag{6.5}$$

where m_0 is the free electron mass. This large value for the oscillator strength is comparable to the value achieved for an intersubband transition in the conduction band of GaAs quantum wells ($f \approx 14$) [Wes85].

6.2.1 Influence of temperature

At this stage it is not clear if the type of confinement in the aligned and elongated dots is that of a quantum wire or a quantum dot. Coupling between the dots could form a quantum wire structure [Pry98]. An approach to test the confinement type is to estimate the population difference between the upper and the ground state assuming either unidimensional subbands or discrete energy levels.

As seen in section 2.3.4, quantum wires and quantum dots are described by different statistics. A Fermi distribution is used for the first, while the latter is described by the Gibbs distribution in the grand canonical ensemble.

The numerical calculations were performed for both systems. For the quantum wires, the calculated decrease of the absorption between $T = 77$ K and $T = 300$ K for an absorption between two levels is 27 %, which is in excellent agreement with the experimental value of 32 %.

However, simulations with the Gibbs distribution for quantum dots can also give a close estimate if one assumes that there are 5 energy levels and 7 electrons in a dot (this value is the electron density divided by the average surface of a dot for the sample M499) and the observed transition occurs between the ground state and the fourth excited level. The problem with these calculations is, that on behalf of the two known energy levels (the ground state and an excited state at $\sim$ 90 meV) the energies of the other three supposed states are unknown. By changing the energy position of these levels, a big range of absorption decrease can be covered.

A clear conclusion cannot be drawn from the performed simulations. However, it is convincing that the simple simulation of the quantum wire with no adjustable parameters gives a very good result.

6.2.2 Polarization-angle dependence

The previous experiments show, that the confinement direction of the excited state is along the x axis, which is perpendicular to the direction of elongation of the dots. Because it has been also shown that the dots present size fluctuations, it would be interesting to test, if fluctuations of the confinement direction of the exited states can be found as well.

Figure 6.8 shows the integrated absorption of the n-doped sample M499 at $T = 300$ K as a function of the light polarization angle θ, with $\theta = 0\,^\circ$ for light polarized along the x axis and $\theta = 90\,^\circ$ for y polarized light. A spectrum of the p-doped sample M500 with same thickness, which has no infrared resonance, served in this case as the background spectrum. The evolution is well fitted by a $\cos^2(\theta)$ law, as it would be expected for dipoles which are aligned parallel

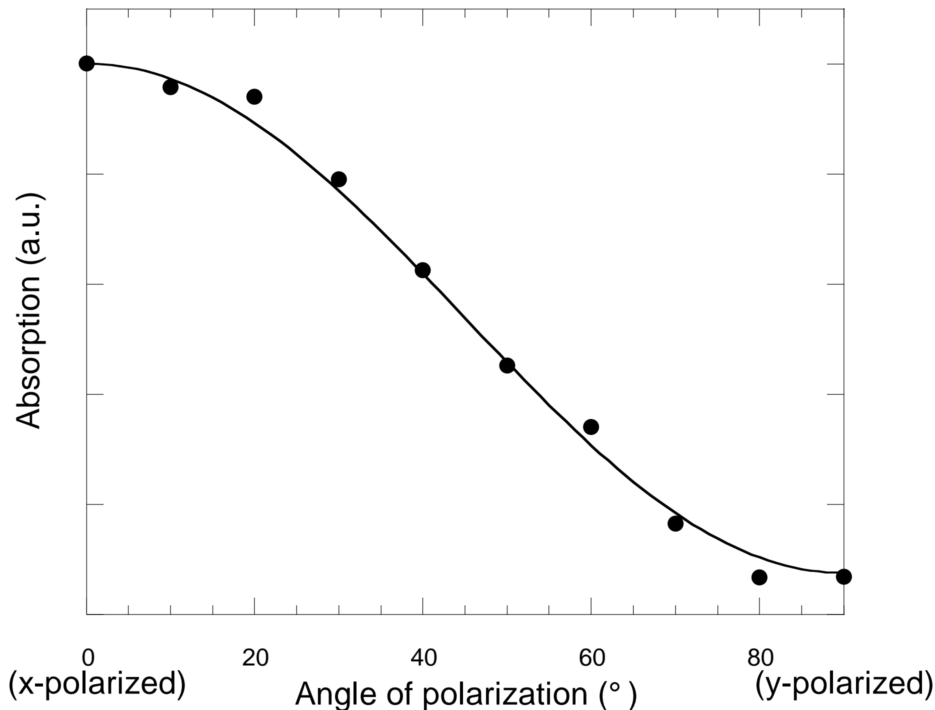

Figure 6.8: Polarization-angle dependence of the integrated infrared absorption of the n-doped sample M499 at $T = 300\,\mathrm{K}$. *The solid line is a calculated* $\cos^2\theta$ *curve.*

to the x axis. It can be concluded that within the experimental precision of ±15 ° the dots are aligned in the same direction and no other confinement direction than x can be found.

6.2.3 Influence of doping density

The question, if the confinement type in the elongated and aligned InAs dots is that of quantum wires or quantum dots, has not been answered until this stage. Assuming the shape and density of quantum dots measured by AFM, there should be an average number of 7 electrons in each dot of sample M499 and 3.5 electrons in each dot of sample M586, based on their respective doping densities. In the case of a quantum dot confinement one would expect the intraband absorption from the ground state to be the same for the samples M499 and M586 because the ground state is already filled by 2 electrons with spin up and spin down.

Figure 6.9 shows the FTIR absorption spectra in x polarization for the two samples in normal incidence configuration at room temperature. The respective spectra in y polarization served as background. The maximum absorption of the sample M499 is $\frac{\Delta t}{t}$ = 5.3 % at 88 meV. Sample

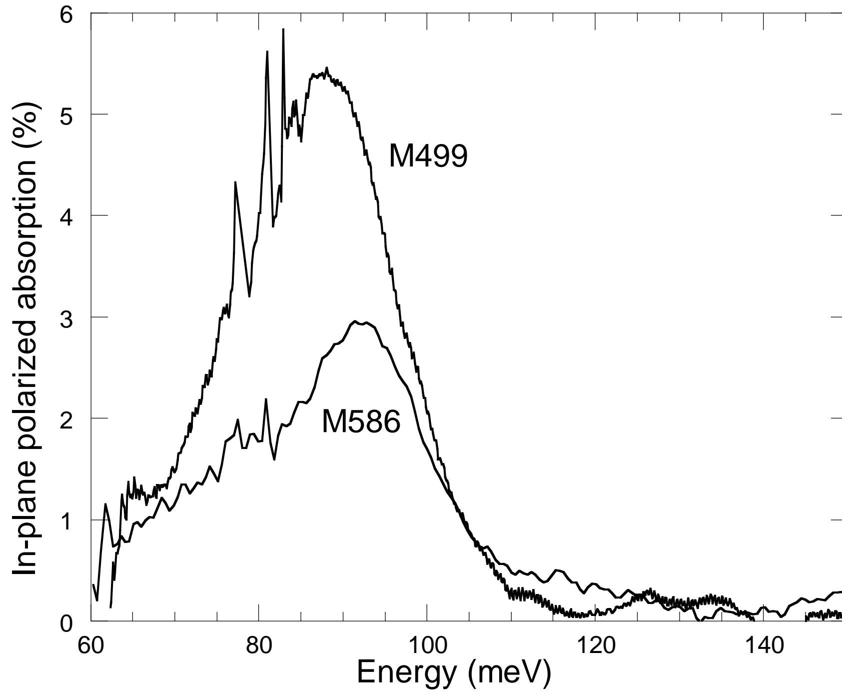

Figure 6.9: Intraband absorption at normal-incidence of the doped samples M499 and M586 at $T = 300$ K.

M586 (with half of the delta doping density of M499) has its maximum absorption $\frac{\Delta t}{t} = 2.9$ % at 92 meV. This means that the absorption grows by a factor ~ 1.8 when the number of carriers in the delta doping layer is doubled. Such behavior is expected for a quantum wire confinement potential because there are always empty states above the Fermi energy in the ground subband.

6.2.4 Conclusion

The FTIR experiments on the doped samples show that the intraband absorption at ~ 90 meV is a transition from the ground electron state to an excited state confined in the layer plane along the x direction. The absorption at normal-incidence is giant since it reaches 7.7 % for only 10 layers of n-doped quantum dots. The oscillator strength of the intraband transition is comparable to that achieved in quantum wells for a conduction band intersubband transition. The dependence of the intraband absorption on carrier concentration and temperature suggests a quantum-wire type confinement potential.

6.3 Spontaneous emission

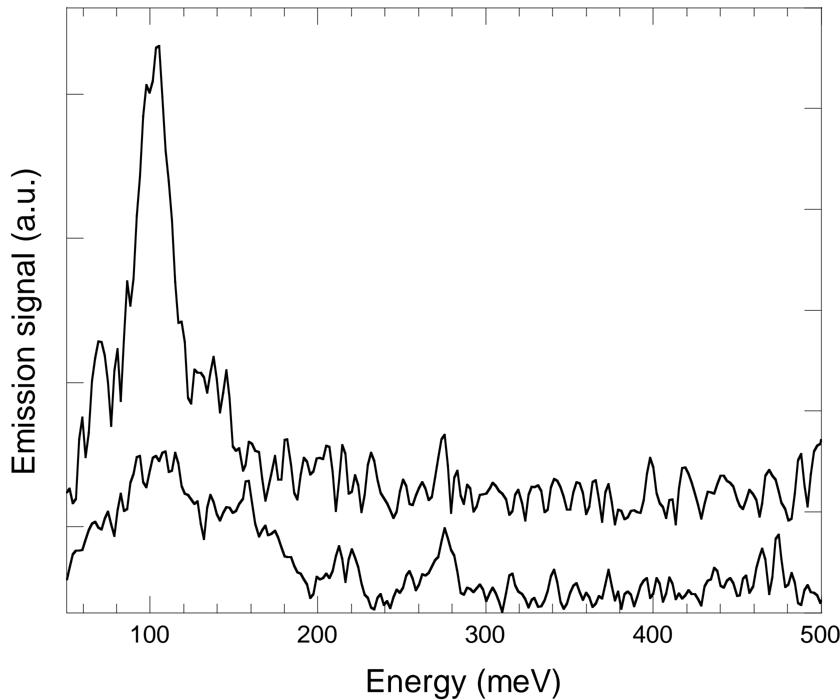

Figure 6.10: Spontaneous emission of the n.i.d. sample M559 at $T = 300$ K *(upper curve). The* Ar^{++} *excitation intensity was* $100\ \frac{\mathrm{W}}{\mathrm{cm}^2}$*. The lower curve represents the black body radiation background of the non excitated sample. The curves are shifted horizontally for better visibility.*

Because of the giant magnitude of the oscillator strength one can expect large intraband absorption or emission for the dots. We now describe preliminary experiments aimed at demonstrating the existence of intraband emission in the quantum dots.

Figure 6.10 shows a FTIR emission spectrum of the undoped sample M559 at $T = 300$ K. The sample was excited by an Ar^{++} laser at normal-incidence to the sample surface with an intensity of $100\frac{\mathrm{W}}{\mathrm{cm}^2}$. The IR emission of the quantum dots was then collected perpendicularly from a facet with a combination of two parabolic mirrors and injected into the FTIR spectrometer in the place of the glow-bar infrared source, which is normally used for transmission spectra (figure 6.11). A Ge filter was installed in front of the MCT detector to cut the strong photoluminescence from the sample. In this configuration, emission spectra of external sources can be carried out with the FTIR spectrometer.

The upper spectrum in figure 6.10 shows the intraband emission of the sample. It is not divided

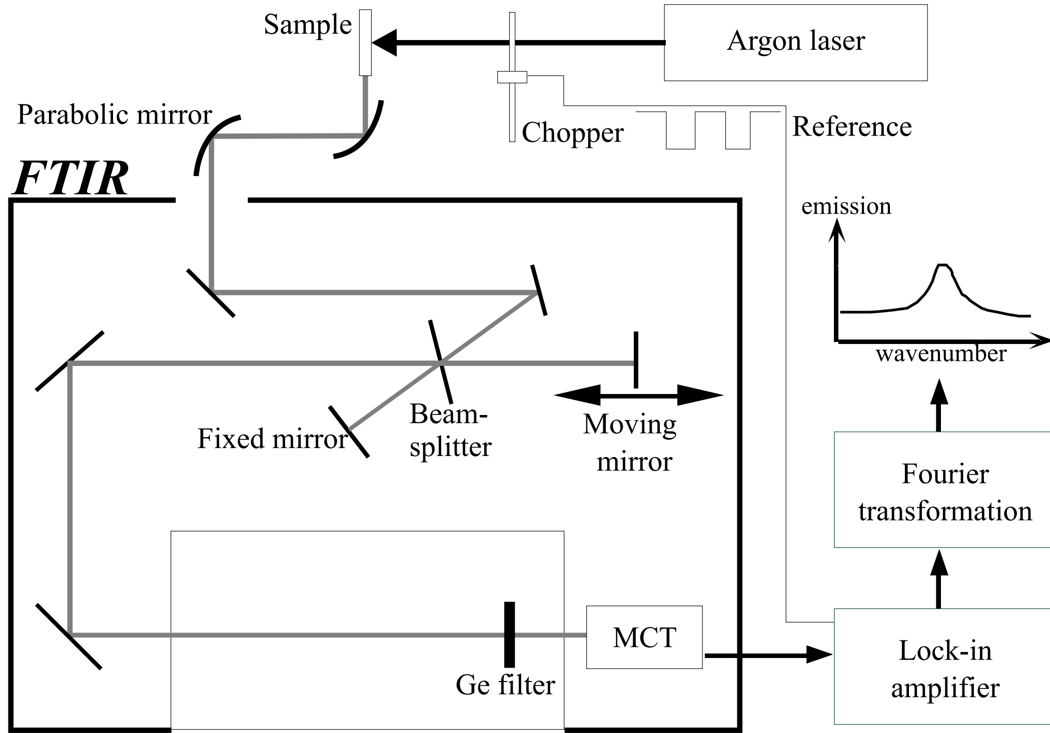

Figure 6.11: Experimental setup for the infrared spontaneous emission experiment.

by the 300 K background spectrum without Ar^{++} laser excitation shown in the lower spectrum. As seen, an intraband emission peaked at 102meV with a FWHM of 22meV is observed. In fact, both experiments (photo-induced emission and emission background) reveal the background black body radiation of the excited or not sample. The black body radiation should have its maximum after the law of Wien

$$\lambda_{\max} = \frac{2.8978 \cdot 10^{-3}\ \mathrm{m} \cdot \mathrm{K}}{T} \tag{6.6}$$

at an energy of $\sim$ 128 meV for a temperature of $T = 300$ K, which is the case within the sensibility of the measurement.

When the quantum dots are populated the black body emission spectrum of the quantum dots should reveal an intraband resonance, since there is an equilibrium between absorption and emission. An alternate way of explaining the observation of 300 K emission from the dots is to consider that electrons are excited thermally in the upper state at 300 K where they can give arise to a spontaneous emission to the electron ground state.

6.4 Conclusion

We have evidenced for the first time a giant intraband absorption in the InAs / $In_{0.52}Al_{0.48}As$ quantum dots. The transition occurs from the ground state to the first excited state confined in the [110] direction in the conduction band. The oscillator strength of the intraband transition is comparable to that achieved in quantum wells for a conduction band intersubband transition. The dependence on carrier density shows the electron confinement type is that of a quantum wire, at least for temperatures above 77 K. This can be explained by the coupling of the elongated and aligned quantum dots in the $[\bar{1}10]$ direction.

Finally, we have demonstrated for the first time that intraband spontaneous emission also does occur.

The InAs / $In_{0.52}Al_{0.48}As$ system may be of great interest for infrared photodetection applications because large absorption quantum efficiencies can be achieved at normal incidence. The fact that intraband emission does occur is extremely promising for the further development of unipolar lasers relying on intraband emission in quantum dots.

Chapter 7

Conclusion

During this Diplomarbeit, self-assemled InAs / $In_{0.52}Al_{0.48}As$ / InP quantum dots have been characterized by atomic force microscopy (AFM), photoluminescene (PL), photoluminescence excitation (PLE) and infrared spectroscopy.

The dots were grown in the Stranski-Krastanov growth mode. The AFM image shows that the wetting layer is almost fully covered with InAs elongated islands of different sizes, which are aligned in the $[\bar{1}10]$ direction. The average size of the dots is 50 nm along $[\bar{1}10]$ and 25 nm along [110] with an average height of only 1.5 nm.

PL spectroscopy confirmes, that the sample contains dots of different volumes. The size distribution of the quantum dots shows five *preferred* dot sizes, each represented by a Gaussian distribution. The origin of the *preferred* sizes could be monolayer fluctuations of the wetting layer during the growth process. High exciting energies show the filling of larger dots and transitions between excited states.

PLE spectra show, that there is only one excited state for each dot size.

Infrared spectroscopy with a Fourier transform infrared (FTIR) spectrometer evidences, for the first time in the InAs / $In_{0.52}Al_{0.48}As$ / InP system, a strong normal-incidence absorption in the quantum dots. The absorption at $\sim$ 90 meV is found to be a transition from the ground electron state to the first excited state confined in the layer plane along the [110] axis. The absorption at normal-incidence reaches 7.7 % for only 10 layers of quantum dots. The oscillator strength is giant and comparable to that of intersubband transitions in quantum wells. The dependence of the intraband absorption on carrier concentration and temperature suggests a quantum wire type confinement potential, which could be formed by coupling of the aligned quantum dots.

Preliminary emission spectroscopy experiments have also been carried out. They reveal the existence of the intraband spontaneous emission from the first excited state to the ground state

in the conduction band.

However, there are still many open questions. Detailed numerical simulations accounting for size and shape of the quantum structure have to be performed to be able to compare experimental data with these simulations.

To confirm whether or not the phonon bottleneck effect takes place in this quantum structure, intraband relaxation time measurements have to be carried out. This could be done either by spatial resolved spectroscopy, where the linewidth of single dots is measured, or by time resolved infrared absorption measurements to directly measure the scattering times.

The normal-incidence intraband absorption of the InAs / $In_{0.52}Al_{0.48}As$ quantum dots is very promising for the future construction of infrared photodetectors with this material system because of the strong oscillator strength of the absorption. The next experiments, which have to be carried out for the development of photodetectors, are photoconduction spectroscopy experiments. This implies the growth of n-i-n structures containing multiple layers of n-doped quantum dots, followed by mesa etched structures.

Because of the large oscillator strength associated with the intraband transition in the InAs / $In_{0.52}Al_{0.48}As$ system, strong infrared emission is possible. Further experiments will be aimed at the demonstration of an intraband population inversion, which is the first step towards the realization of unipolar lasers relying on quantum dots.

Appendix A

Material parameters

The most important material parameters for the InAs / $In_{0.52}Al_{0.48}As$ / InP system are [Cas84, Fra94, Gen97, Bas95]:

	InAs	$In_{0.52}Al_{0.48}As$	InP
lattice constant a	6.05 Å	5.87 Å	5.87 Å
Energy gap E_g(300 K)	0.354 eV	1.415 eV	1.344 eV
Energy gap E_g(0 K)	0.417 eV	1.520 eV	1.424 eV
Effective mass m_e^*	0.027 m_0	0.084 m_0	
Effective mass m_{hh}^*	0.6 m_0	0.68 m_0	
Effective mass m_{lh}^*	0.027 m_0	0.086 m_0	
Elastic constant c_{11}	$8.33 \cdot 10^6 \frac{N}{cm^2}$		
Elastic constant c_{12}	$4.53 \cdot 10^6 \frac{N}{cm^2}$		
Elastic constant c_{44}	$3.99 \cdot 10^6 \frac{N}{cm^2}$		
Conduction band deformation potential a	$-5.9 \cdot 10^5 \frac{eV \cdot cm^2}{N}$		
Valence band deformation potential b	$-1.8 \cdot 10^5 \frac{eV \cdot cm^2}{N}$		
Refractive index $\tilde{n}$ at E_g	~ 3.52	~ 3.36	3.450

The energy band discontinuity at $T = 300$ K between strained InAs and $In_{0.52}Al_{0.48}As$ is [Gen97]:

$$\Delta E_{\text{conduction}} = 0.63 \text{ eV},$$
$$\Delta E_{\text{valence}} = 0.43 \text{ eV}.$$

The phonon energies of InP at $T = 77$ K are [Sti64]:

$$\hbar\omega_{\mathrm{TO}} = 38.5 \text{ meV},$$
$$\hbar\omega_{\mathrm{LO}} = 42.0 \text{ meV}.$$

Bibliography

[Abs79] G. Abstreiter, K. Ploog, *Phys. Rev. Lett.* 42, p. 1308 (1979). 1

[All88] P. von Allmen, M. Berz, G. Petrocelli, F.-K. Reinhart, G. Harbeke, *Semicond. Sci. Technol.* 3, p. 1211 (1988). 52

[Ara82] Y. Arakawa, H. Sakaki, *Appl. Phys. Lett.* 40, p. 939 (1982). 14

[Ave91] D.V. Averin, A.N. Korotkov, K.K. Likharev, *Phys. Rev. B* 44, p. 6199 (1991). 23

[Bas88] G. Bastard, *Wave mechanics applied to semiconductor heterostructures*, les éditions de physique, France (1988). 16, 18, 19

[Bas94] G. Bastard, *Phys. Rev. Lett.* 73, p. 716 (1994). 38

[Bas95] M. Bass, *Handbook of Optics*, 2. edition, Volume II (1995). 61

[Ben91] H. Benisty, C.M. Sotomayor-Torres, C. Weisbuch, *Phys. Rev. B* 44, p. 10945 (1991). 38, 42

[Boc90] U. Bockelmann, G. Bastard, *Phys. Rev. B* 42, p. 8947 (1990). 42

[Boc92] U. Bockelmann, T. Egeler, *Phys. Rev. B* 46, p. 15574 (1992). 42

[Boc93] U. Bockelmann, *Phys. Rev. B* 48, p. 17637 (1993). 42

[Bee91] C.W.J. Beenakker, *Phys. Rev. B* 44, p. 1646 (1991). 23

[Bra98] J. Brault, M. Gendry, G. Grenet, G. Hollinger, Y. Desieres, T. Benyattou, to be published (1998). 27

[Cas84] H.C. Casey, M.B. Panish, *Heterostructure Lasers, Part B: Materials and Operating Characteristics*, Academic Press, United States (1984). 61

[Cha89] Y.C. Chang, R.B. James, *Phys. Rev. B* 39, p. 12672 (1989). 20

[Chu91] S.L. Chuang, *Phys. Rev. B* 43, p. 9649 (1991). 9, 10

[Cus96] M.A. Cusack, P.R. Briddon, M. Jaros, *Phys. Rev. B* 54, p. R2300 (1996). 11

[Cus97] M.A. Cusack, P.R. Briddon, M. Jaros, *Phys. Rev. B* 56, p. 4047 (1997). 11

[Dre94] H. Drexler, D. Leonard, W. Hansen, J.P. Kotthaus and P.M. Petroff, *Phys. Rev. Lett.* 73, p. 2252 (1994). 32

[Fra94] C. Francis, *Thèse*, Université de Paris-Sud (1994). 9, 27, 61

[Gen97] M. Gendry, *Data sheets of sample growth parameters*, furnished with the samples (1997). 26, 61

[Gru95] M. Grundmann, O.Stier, D. Bimberg *Phys. Rev. B* 52, p. 11969 (1995). 11, 12, 26

[Gru97] M. Grundmann, D. Bimberg, *Phys. Bl.* 53, Nr. 6, p. 517 (1997). 25

[Iko89] Z. Ikonic, V. Milanovic, D. Tjapkin, *Solid State Comm.* 72, p. 835 (1989). 22

[Ino92] T. Inoshita, H. Sakaki, *Phys. Rev. B* 46, p. 7620 (1992). 42

[Jul91] F.H. Julien, P. Vagos, J.-M. Lourtioz, D.D. Yang, R. Planel, *Appl. Phys. Lett.* 59, p. 2645 (1991). 32

[Kam74] A. Kamgar, P. Kneschaurek, G. Dorda, J.F. Koch, *Phys. Rev. Lett.* 32, p. 1251 (1974). 1

[Kan75] E.O. Kane, *J. Phys. Chem. Solids* 1, p. 249 (1975). 8

[Khu92] J. Khurgin, *Appl. Phys. Lett.* 62, p. 1390 (1992). 21

[Lip95] H. Lipsanen, M. Sopanen, J. Ahopelto, *Phys. Rev. B* 51, p. 13868 (1995). 38

[Mar94] J.-Y. Marzin, G. Bastard, *Solid State Commun.* 92, p. 437 (1994). 11

[Mou96] Z. Moussa, *Thèse*, Université de Paris-Sud (1996). 16

[Muk96] K. Mukai, N. Ohtsuka, H. Shoji, M. Sugawara, *Appl. Phys. Lett.* 68, p. 3013 (1996). 38, 42

[Nak87] K. Nakashima, Y. Kawaguchi, Y. Kawamura, H. Asahi, Y. Imamura, *Japn. J. Appl. Phys.* 26, p. L1620 (1987). 27

[Pin79] A. Pinczuk, H.L. Störmer, R. Dingle, J.M. Worlock, W. Wiegmann, A.C. Gossard, *Solid State Commun.* 32, p. 1001 (1979). 1

[Pry98] C. Pryor, *Phys. Rev. Lett.* 80, p. 3579 (1998). 53

[Sau97] S. Sauvage, P. Boucaud, F.H. Julien, J.M. Gérard and J.-Y. Marzin, *J. Appl. Phys.* 82, p. 3392 (1997). 2, 32, 38

[Sti64] D.L. Stierwalt, R.F. Potter, *Physics of semiconductors: proceedings of the 7th international conference*, Dunod, Paris, p.1073 (1964). 62

[Vag94] P. Vagos, *Thèse*, Université de Paris-Sud (1994). 8

[Wes85] L.C. West, S.J. Eglash, *Appl. Phys. Lett.* 46, p. 1156 (1985). 1, 52

[Wu96] L. Wu, *Thèse*, Université de Paris-Sud (1996). 33

[Yan91] D. Yang, *Thèse*, Université de Paris-Sud (1991). 21

[Zun98] A. Zunger, *MRS Bulletin* Vol. 23 No. 2, p. 35 (1998). 11, 13

Acknowledgements

I would like to thank all the persons who supported me during this Diplomarbeit:

- Dr. François H. Julien for giving me the great opportunity to work in his group at the IEF and for his always available support and care of me.
- Prof. Dr. A. Forchel for making this external Diplomarbeit possible and for helping me whenever I asked.
- Olivier Gauthier-Lafaye for many discussions, explanations and help whenever needed.
- Dr. J.M. Lourtioz for welcoming me in CROQ.
- Stéphane Cabaret for always quickly finding the right solution for all mechanical and electrical problems.
- All the other staff and Ph.D. students in CROQ for always supporting me and for our fruitful discussions during coffee breaks.
- Dr. M. Gendry for extensive collaboration as well as growing the samples and making the AFM images.
- Dr. T. Benyattou for carrying out the PLE and some high resolution PL spectra.

Erklärung

Hiermit erkläre ich, daß ich die vorliegende Arbeit selbständig verfaßt und keine anderen als die angegebenen Quellen und Hilfsmittel benutzt habe.

Würzburg, den 14. August 1998,

Alexander Weber